JGR Solid Earth

RESEARCH ARTICLE
10.1029/2020JB020701

Key Points:

- 3D Vp and Vp/Vs models were calculated using local earthquake tomography in the region affected by the 2016 Pedernales, Ecuador earthquake
- Tomographic images highlight the heterogeneities of the margin affected by seamounts and ridges comprising the oceanic crust
- Carnegie Ridge seems the main feature controlling the seismic activity and the offshore extent of large megathrust earthquakes in the region

Supporting Information:

- Supporting Information S1

Correspondence to:
S. León-Ríos,
sergio.leon-rios@kit.edu

Citation:
León-Ríos, S., Bie, L., Agurto-Detzel, H., Rietbrock, A., Galve, A., Alvarado, A., et al. (2021). 3D local earthquake tomography of the Ecuadorian margin in the source area of the 2016 Mw 7.8 Pedernales earthquake. *Journal of Geophysical Research: Solid Earth*, *126*, e2020JB020701. https://doi.org/10.1029/2020JB020701

Received 4 AUG 2020
Accepted 27 FEB 2021

3D Local Earthquake Tomography of the Ecuadorian Margin in the Source Area of the 2016 Mw 7.8 Pedernales Earthquake

Sergio León-Ríos[1], Lidong Bie[1], Hans Agurto-Detzel[2], Andreas Rietbrock[1], Audrey Galve[2], Alexandra Alvarado[3], Susan Beck[4], Philippe Charvis[2], Yvonne Font[2], Silvana Hidalgo[3], Mariah Hoskins[5], Mireille Laigle[2], Davide Oregioni[2], Anne Meltzer[5], Mario Ruiz[3], and Jack Woollam[1]

[1]Karlsruhe Institute of Technology, Geophysical Institute, Karlsruhe, Germany, [2]Université Côte d'Azur, IRD, CNRS, Observatoire de la Côte d'Azur, Géoazur, Nice, France, [3]Instituto Geofisico, Escuela Politécnica Nacional, Quito, Ecuador, [4]Department of Geosciences, University of Arizona, Tucson, AZ, USA, [5]Department of Earth and Environmental Sciences, Lehigh University, Bethlehem, PA, USA

Abstract Based on manually analyzed waveforms recorded by the permanent Ecuadorian network and our large aftershock deployment installed after the Pedernales earthquake, we derive three-dimensional Vp and Vp/Vs structures and earthquake locations for central coastal Ecuador using local earthquake tomography. Images highlight the features in the subducting and overriding plates down to 35 km depth. Vp anomalies (~4.5–7.5 km/s) show the roughness of the incoming oceanic crust (OC). Vp/Vs varies from ~1.75 to ~1.94, averaging a value of 1.82 consistent with terranes of oceanic nature. We identify a low Vp (~5.5 km/s) region extending along strike, in the marine forearc. To the North, we relate this low Vp and Vp/Vs (<1.80) region to a subducted seamount that might be part of the Carnegie Ridge (CR). To the South, the low Vp region is associated with high Vp/Vs (>1.85) which we interpret as deeply fractured, probably hydrated OC caused by the CR being subducted. These features play an important role in controlling the seismic behavior of the margin. While subducted seamounts might contribute to the nucleation of intermediate megathrust earthquakes in the northern segment, the CR seems to be the main feature controlling the seismicity in the region by promoting creeping and slow slip events offshore that can be linked to the updip limit of large megathrust earthquakes in the northern segment and the absence of them in the southern region over the instrumental period.

Plain Language Summary Using seismic data recorded by the permanent Ecuadorian network and the large emergency installation after the 2016 Pedernales earthquake, we obtained the seismic velocity structure together with precise earthquake locations for the coastal Ecuadorian margin. Our images highlight the heterogeneities of the subduction zone affected by seamounts and ridges comprising the oceanic crust. These features play an important role in controlling the seismic behavior of the margin. While seamounts can contribute to the occurrence of intermediate (M ~ 7–7.5) megathrust earthquakes in the north, the Carnegie Ridge seems to be the main feature controlling the seismicity in the region by promoting creeping and slow slip events offshore that can be linked to the updip limit of large megathrust earthquakes in the northern segment and the absence of them in the southern region.

1. Introduction

The subduction margin of Ecuador presents a structural segmentation along strike mainly caused by subducting topography coming from the oceanic plate (e.g., Collot et al., 2002; Gailler et al., 2007; Marcaillou et al., 2016). Additionally, the margin hosts a wide variety of seismic behavior including large megathrust earthquakes, seismic swarms, repeating earthquakes, and slow slip events (SSE, e.g., Agurto-Detzel et al., 2019; Font et al., 2013; Rolandone et al., 2018). To the north of the equator, the margin has produced several large magnitude ≥7.5 subduction earthquakes in the past (Abe, 1979; Beck & Ruff, 1984; Herd et al., 1981; Kanamori & McNally, 1982; Kelleher, 1972; Mendoza & Dewey, 1984; Ramírez, 1975; Sennson & Beck, 1996). South of the equator, just a small number of large subduction earthquakes have been observed (Bilek, 2010; Dorbath et al., 1990; Egred, 1968), with only two Mw > 7.0 events that occurred close to Bahia Caraquez (Storchak et al., 2013), and seismic activity has been mostly associated with swarms

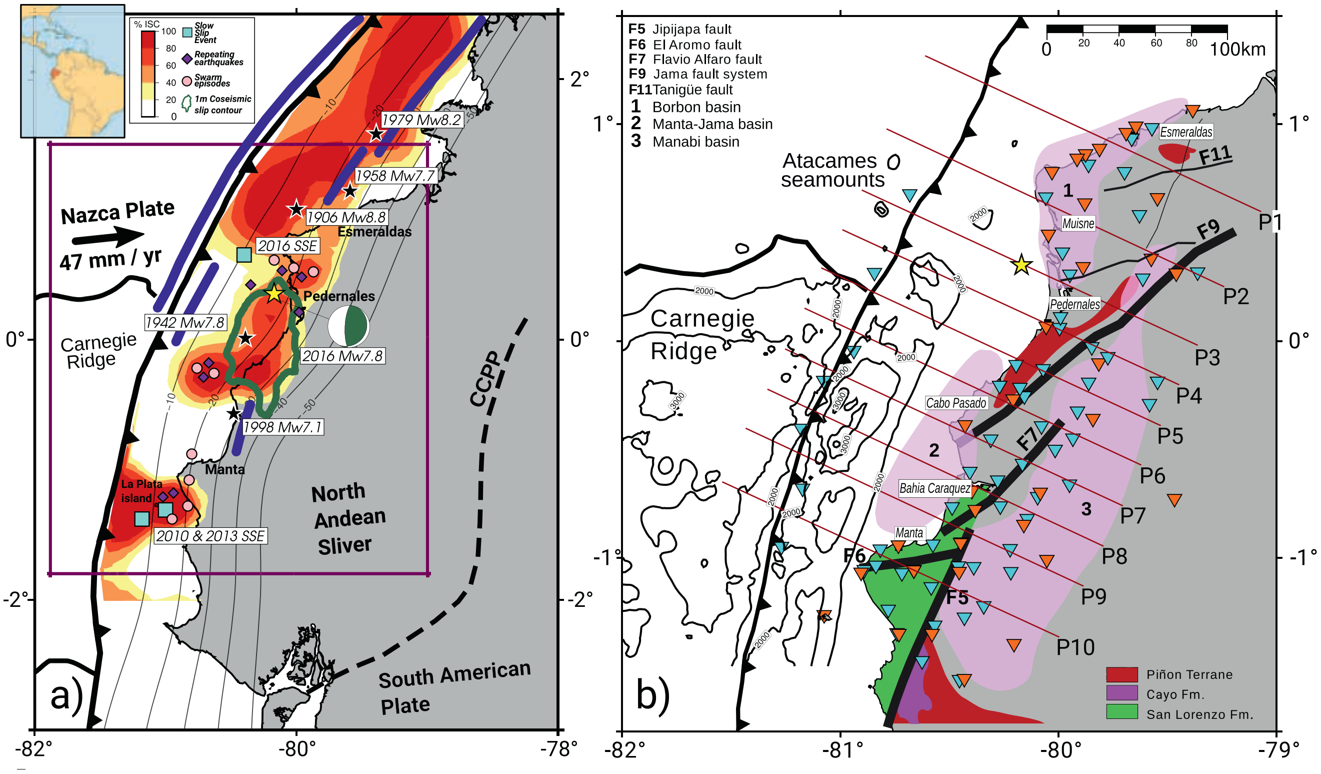

Figure 1. Seismotectonic and geological setting. (a) Seismotectonic setting of the study area. Solid blue lines represent the extension of historical earthquakes in the area. Epicenters of those events are indicated with a black star. Slow slip events, repeating earthquakes, and seismic swarm episodes are also represented by squares, diamonds, and circles, respectively. 2016 Pedernales earthquake is shown including its epicenter (yellow star), coseismic slip by Nocquet et al. (2017) (solid green line), and focal mechanism (green beach ball). Distribution of the interseismic coupling by Nocquet et al. (2014). Chingual–Cosanga–Pallatanga–Puna fault (CCPP) that created the North Andean Sliver (NAS) is represented by a segmented line. (b) Geological context and recording network. Main formations, sedimentary basins, and faults mapped by Reyes and Michaud (2012) are displayed by coloring forms and solid black lines. Offshore, residual bathymetry derived by Agurto-Detzel et al. (2019) is shown in solid black line. Permanent Ecuadorian network (RENSIG, Alvarado et al., 2018) and emergency deployment (Meltzer et al., 2019) are shown in orange and light blue inverted triangles, respectively. Profiles, P1–P10, discussed in this work are plotted in solid red line. Yellow star represents the epicenter of the 2016 Pedernales earthquake (Nocquet et al., 2017).

(Segovia, 2001; Segovia et al., 2009; Vaca et al., 2009), repeating earthquakes (Rolandone et al., 2018) and SSE (Chlieh et al., 2014; Collot et al., 2017; Mothes et al., 2013; Rolandone et al., 2018; Segovia et al., 2018; Vaca et al., 2018; Vallée et al., 2013). The Mw 7.8 Pedernales earthquake occurred in 2016 and was located in a region previously identified as highly coupled by Chlieh et al. (2014). Nocquet et al. (2017) showed that an area of about 100 × 40 km^2 was affected by coseismic slip (see Figure 1a). The associated after-slip was described by Rolandone et al. (2018) highlighting that areas surrounding the mainshock experienced postseismic slip and SSE. This phenomenon, where several types of slip behavior are capable of coexisting during interseismic, coseismic, and postseismic stages, suggests a highly heterogeneous plate boundary.

Although the Ecuadorian margin has been widely studied, there is still no consensus about a regional scale 3D velocity model (3DVM), especially for the coastal area and the marine forearc, where megathrust earthquakes pose high seismic hazard. Previous local studies in the Esmeraldas segment (Agudelo et al., 2009; Gailler et al., 2007; Garcia-Cano et al., 2014), La Plata island (Gailler et al., 2007), and part of the Carnegie Ridge (CR) (Gailler et al., 2007; Graindorge et al., 2004; Sallarès & Charvis, 2003; Sallarès et al., 2005) have contributed to our understanding of the first-order characteristics of the physical properties of the margin. On a regional scale, Font et al. (2013) built a velocity model for the forearc by combining geodynamic, structural, and velocity data, reproducing the slab geometry. Araujo (2016) derived a seismic velocity model and Moho depth for a larger area based on seismic data from the Ecuadorian permanent network (RENSIG); however, small-scale structures (e.g., seamounts) that could impact the seismic behavior in the forearc region were not resolved. Lynner et al. (2020) and Koch et al. (2020) used ambient noise and joint ambient noise and receiver function methods respectively to image the coastal forearc but were unable to image the marine forearc together with the *P* wave velocity in the region.

Based on the aftershock activity of the April 16, 2016, Pedernales earthquake and the background seismic activity recorded by our temporary seismic network, which included ocean bottom seismometers (OBSs) installed along the trench axis (León-Ríos et al., 2019; Meltzer et al., 2019), we derive a novel 3DVM for Vp and Vp/Vs together with precise hypocentral locations for the central coastal area of Ecuador. Local earthquake tomography images the physical properties of the margin which, together with the regional seismotectonic and geological settings, provide a descriptive interpretation of the major features involved in the Ecuadorian subduction process. Our findings highlight not only a very heterogeneous margin with seamounts and large bathymetric features within the oceanic crust but also an overriding plate highly affected by large-scale faults. Finally, we discuss how these structures might contribute to controlling the seismic activity in the Ecuadorian margin.

2. Tectonic Setting

The Ecuadorian margin is controlled by the subduction of the oceanic Nazca plate beneath the continental South American plate. This process occurs with an east–west convergence rate of ~47 mm/year (Kendrick et al., 2003; Nocquet et al., 2009, 2017; Trenkamp et al., 2002). The margin has been recognized as highly segmented and mainly erosional (Collot et al., 2002; Gailler et al., 2007; Marcaillou et al., 2016). The continental forearc is divided by the Chingual–Cosanga–Pallatanga–Puna (CCPP) fault zone (Alvarado et al., 2016), limiting the North Andean Sliver (NAS) as shown in Figure 1a. In front of the NAS, the Nazca plate is less than 26 Ma old (Lonsdale, 2005) and subducts at a relative rate of about 46 mm/year (Chlieh et al., 2014).

Offshore, the study area is characterized by the presence of large bathymetric features such as the aseismic CR, the Atacames seamount chain, and, farther north, the Yaquina graben interpreted as an extinct rift and transform fault closer to the trench (Hardy, 1991; Lonsdale, 2005) (see Figure 1b). These significant along-strike and along-dip structural variations, which might exist at greater depth on the subducted portion of the plate, may contribute to the diverse patterns of seismicity along strike (Agurto-Detzel et al., 2019; Font et al., 2013; Gailler et al., 2007). The CR subducts beneath the Ecuadorian trench between latitude ~1°N and ~2°S (see Figure 1). It is ~280 km wide and 2 km high and is currently subducting in ENE direction. Residual bathymetry (Figure 1b) derived by Agurto-Detzel et al. (2019) images the rough topography caused by the CR. The CR was formed by the Galapagos hot-spot (GHS) located about 1,000 km west of the coastline of Ecuador. At the northern flank of the CR, a series of seamounts, including the Atacames seamounts, are subducting beneath the South American plate. Marcaillou et al. (2016) point out that the Atacames seamounts play an important role on promoting the stable sliding of the updip segment of the seismogenic zone and controlling the propagation of large subduction earthquakes toward the trench. The thickness of the oceanic crust varies along strike—from 5 km in the north, close to Esmeraldas (~1°N), to 14 km in the south (~1°S), reaching its maximum of 19 km beneath the crest of the CR (Calahorrano et al., 2008; Garcia-Cano et al., 2014; Graindorge et al., 2004; Meissnar et al., 1976; Sallarès & Charvis, 2003; Sallarès et al., 2005).

Toward the coast, the current forearc in central Ecuador is the result of subsequent accretion of lithospheric material and arc rocks that occurred between the late Cretaceous to the Paleocene/Eocene (Jaillard et al., 2009; Reynaud et al., 1999). A thin layer of sediments of 500–1,000 m (Jaillard et al., 2000) covers most of the forearc. Distributed along the coastline, magmatic outcrops have been associated with the Piñon formation (Luzieux et al., 2006; Reyes & Michaud, 2012; Reynaud et al., 1999) which is identified as "the Cretaceous igneous basement of western Ecuador" (Reynaud et al., 1999) and extends along the whole study area up to the CCPP fault to the east. In the Manta area, the San Lorenzo block, a mix of volcanic conglomerates, appears in conformity with the Piñon formation (Reyes & Michaud, 2012; Reynaud et al., 1999) creating oceanic terranes. Quaternary sediments cover these as well as other small formations, forming several basins along the coast such as the Borbon, Manta–Jama, and Manabi basin (see (1), (2), and (3) in Figure 1b). The local tectonic and seismic activity is controlled by major faults that bound these basins (Agurto-Detzel et al., 2019; Font et al., 2013; León-Ríos et al., 2019; Luzieux et al., 2006; Reyes & Michaud, 2012; Reynaud et al., 1999; Soto-Cordero et al., 2020). Reyes and Michaud (2012) updated the coastal geological map for Ecuador extending several faults observed at the surface. The main geological structures and faults (Figure 1b) not only contribute to regional tectonic control but also allow the circulation of fluids within the margin (e.g., the Jipijapa fault; Segovia et al., 2018).

3. Network and Data Set

3.1. The Seismic Aftershock Network

After the 2016 Pedernales mainshock, a large international collaboration coordinated a rapid response to install a temporary seismic network (Meltzer et al., 2019). One month after the mainshock, a dense temporary amphibious network was deployed comprising broadband and short period seismic land stations and OBS stations along the trench. Figure 1b shows the spatial distribution of the final deployment, including both temporary and permanent deployments consisting on more than 80 stations, with a station spacing of approximately 10–30 km. Onshore stations were fully operative from May 2016 to June 2017. Offshore, OBSs were recording between mid-May and November in 2016.

3.2. Data Set

To extend the catalog prepared to obtain the 1D velocity model (León-Ríos et al., 2019), we incorporated additional events from the refined earthquake catalog by Agurto-Detzel et al. (2019). Seismicity with $M_L \geq 2.5$ recorded between May and November 2016 and located in the vicinity (300×200 km^2) of the temporary network was included in the 3D inversion process. From this catalog, *P* and *S* wave arrival times were manually picked using the Seismic Data eXplorer (SDX) software package (Heath, 2010) that utilizes a modified hypo71 algorithm for the hypocenter location (Lee & Lahr, 1972). Following the procedures from Agurto et al. (2012), Hicks et al. (2014), and León-Ríos et al. (2019), we assigned pick error categories, referred as weights, from 0 to 4 to describe the quality of the selected arrival times. Each weight corresponds to the following time uncertainties: Weight 0 (<0.04 s), Weight 1 (0.04–0.1 s), Weight 2 (0.1–0.2 s), Weight 3 (0.2–1 s), and Weight 4 (>1 s). Events were located using the minimum 1D model and station correction terms from León-Ríos et al. (2019). Finally, we accepted 568 events with at least 10 P- and 5 S-phase observations. The range in azimuthal gap is between 46° and 210° for 549 earthquakes. Close to the trench, in the northernmost region, we relaxed the restriction for events with an azimuthal gap <230°, as otherwise the earthquake distribution would have become uneven. The final catalog contains 10,628 P-phases and 9,134 S-phases with a median azimuthal gap of 123°.

4. Method: Local Earthquake Tomography

Following the procedure detailed by, for example, Husen et al. (2000), Haberland et al. (2009), and Hicks et al. (2014), we performed a series of iterative travel time inversions to obtain Vp, Vp/Vs, and hypocentral locations using SIMULPS (Eberhart-Phillips, 1990; Evans et al., 1994; Thurber, 1983, 1993). To compute seismic velocities and hypocentral parameters, the algorithm performs iterative travel time inversions within a 3D nonregular nodal grid defined by the user. For our inversion, we defined a grid of $200 \times 250 \times 60$ km^3 (see Figure S1) with nodes organized in profiles perpendicular to the trench axis. The 1D velocity model (León-Ríos et al., 2019; see Figure S2) represents the structure of the margin below a reference station located at the coast, approximately where northern limit of the CR subducts. To ensure, this does not bias our 3D results and because of the margin segmentation (Gailler et al., 2017), we followed a graded approach (e.g., Eberhart-Phillips, 1986; Husen et al., 2000; Roecker, 1993; Thurber et al., 1995, among others) and invert for a coarse 2D velocity model (2DVM) and precise earthquake localization in two segments located north and south of the equator. The refined locations and associated travel time observations were merged for the subsequent 3D inversion. For all stages, damping values were derived by analyzing trade-off curves (Eberhart-Phillips, 1986; see Figure S3). *P* wave velocities were initially calculated and then used as input to perform the Vp/Vs inversion. We applied a staggered grid approach by shifting the coordinate system of the inversion nodes by a third to improve our lateral resolution as has been previously suggested (e.g., Collings et al., 2012; Haberland et al., 2009; Hicks et al., 2014). A detailed description of each step is given in the following sections.

4.1. Two-Dimensional Modeling

To obtain the 2DVM, we extended our minimum 1D model (León-Ríos et al., 2019) along a 2D grid with a west-east orientation perpendicular to the trench. In depth, the distance between nodes follows the layering of the minimum 1D model and varies from 2.5 km at shallower layers to 10 km at greater depths (see Figures S1 and S2). To obtain a spatially even event distribution and to increase the amount of P- and S-onsets for the inversion, we augmented the 1D catalog (León-Ríos et al., 2019) of 227 earthquakes with 222 manually picked events to obtain a catalog of 549 earthquakes (≥10 P-onsets, ≥5 S-onsets, and gap < 210°). To account for the structural differences between areas located north and south of the equator, we split the analysis in two sections to obtain robust earthquake locations at this initial stage. For the inversion to the north (2D-N), we used 317 events with 5,479 P- and 4,559 S-onset phases. For the south section (2D-S), a total of 232 events containing 4,821 P- and 4,128 S- onset phases were used. Several damping values were tested to select the best one to perform the inversions (see Figure S3). As to our knowledge, no seismic velocity tomography has been carried out and also an accepted model for the slab geometry is still debated in our study region, we started with a rough (average nodal spacing of 25 km) 2D model to improve earthquake locations and to obtain the overall structure of the arc. This was followed by an inversion of a finer 2D grid (horizontal grid spacing of 15 km equivalent to the stations spacing ~15–20 km) to enhance along-strike resolution perpendicular to the trench. For both north and south sections, we applied a staggered grid technique (e.g., Evans & Achauer, 1993; Hicks et al., 2014) by shifting nodes by a third of their minimum spacing along strike to further improve lateral resolution and to allow the seismic velocities to become independent of the actual node locations. The resulting averaged Vp models were then used as the new starting models to invert for Vp/Vs for the north and south cross sections.

4.2. Three-Dimensional Modeling

Using the results from the previous stage, we subsequently calculate a 3DVM. We added 19 additional events to the northernmost part of our study region and close to the trench to achieve a more even raypath coverage in this area of the model and therefore relaxed the azimuthal gap to <230° to be able to incorporate these events. In total, we inverted 568 earthquakes with 10,628 P- and 9,134 S-phases over a 3D grid that comprises 11 profiles with nodes distributed in a volume with a minimum spacing, of 15, 20, and 2.5 km, for the x (east), y (north), and z (down) axis, respectively (see Figure S1). Optimal damping value was again determined by trade-off curve analysis (see Figure S3). The Vp velocities were solved using a smooth 2D starting model that incorporates the slab geometry derived in the previous stage (see Figure S4). Subsequently, we inverted for the 3D Vp/Vs ratios following the same procedure conducted at the 2D modeling stage.

5. Resolution

Although the setting of our amphibious experiment ensures a good recording coverage for the seismicity (see Figure S5), the irregular distribution of both stations and earthquakes raises the problem of resolution heterogeneity within the 3D volume. To identify areas that are well resolved and to distinguish them from areas that are poorly resolved, we conducted several resolution tests. First, following Eberhart-Phillips (1993) and Eberhart-Phillips and Michael (1998), we inspected critical parameters from the model resolution matrix (MRM). By taking the ratio between off-diagonal and diagonal elements of the MRM, we derived the spread function (SF; Michelini, 1991; Michelini & McEvilly, 1991; Toomey & Foulger, 1989) to identify areas with good and poor ray coverage. We also inspected the size and orientation of lateral smearing by contouring the 70% value of the diagonal elements at each row of the MRM (e.g., Collings et al., 2012; Haberland et al., 2009; Hicks et al., 2014; Toomey & Foulger, 1989). In general, large diagonal elements of the MRM, small SF, and rounded contour lines around the grid nodes are indicative of well-resolved areas.

Additionally to inspecting the MRM, we also evaluate synthetic reconstruction tests to identify the well-resolved areas. We started with a classic tool to explore this matter by performing a checkerboard test (Spakman & Nolet, 1988). This type of analysis helps us to estimate how well resolved are different sizes of anomalies in our model and how well amplitudes are recovered and therefore helps to determine the minimum resolvable node spacing. Synthetic travel times were calculated using the observations from our final 3D inversion over an alternating pattern of positive and negative anomalies of 5% of the inverted model.

Different sizes of anomalies (15 and 30 km, see Figures 4 and S8) were tested. Then, the inversion workflow was applied to recover the original structure. Finally, we evaluated the agreements (dv) between the anomalies in the initial and final models.

Furthermore, we performed characteristic model restoring tests to assess the ability to recover features similar to key ones observed in 3DVM and discussed in greater detail later. We focused on the analysis of a subducting seamount shaped with a low Vp anomaly and located close to the trench in profiles P4 and P5. The synthetic model also included a low Vp feature at ~20 km depth, located in P7 (see Figures 4c and S9). Synthetic travel times were computed and subsequently inverted using the initial 2DVM used at the 3D modeling stage. To check the dependency of the initial 2D model on our 3D inversion results, we conducted restoring tests using the 2D-N model and a merged 2D-N and 2D-S model as an initial input for the inversion. For the first case, synthetic travel times were calculated for the 2D-N model projected along the grid (see Figure S10). For the second test, we inverted our actual travel times data set using a 2D model formed by the merging the 2D-N and 2D-S velocity parameters (see Figures S11 and S12). In both cases, the inversions were performed following the same workflow as described for the 3D modeling stage. Additionally, a synthetic test was carried out to assess the restoring capability of our results by using a completely different approach for representing the model and calculating synthetic travel times. Following Podvin and Lecomte (1991), we applied a three-dimensional finite difference ray tracer to calculate travel times over a 500-m grid spacing synthetic models that included the slab geometry and a fast (~7.5 km/s) or slow (~5.5 km/s) Vp anomaly located offshore, around P4. To incorporate uncertainties in the arrival times, Gaussian noise was added based on the weighted variance of each phase (0.05 s for P and 0.1 s for S) based on the average estimated picking accuracy of the manual travel time data set. We reproduced the whole inversion workflow, by starting the inversion using the minimum 1D model (León-Ríos et al., 2019) to restore the slab geometry in the region. Subsequently, travel times were inverted using a coarse grid with only two profiles in the *y* axis and followed by the 3D velocity inversion (see Figures S13 and S14).

Finally, to estimate the uncertainties in the velocity determination, we also performed a bootstrap test by randomly creating 100 subsets of data comprising 80% of the actual catalog which were subsequently inverted. We calculated the standard deviation at each node of the grid (see Figure S15) to estimate the errors of our obtained Vp and Vp/Vs models.

5.1. Model Resolution Matrix

Figures 2 and 3 show the resolution of our 2DVM and 3DVM for both Vp and Vp/Vs. We consider well recovered areas when SF < 65% of its maximum value (e.g., Haberland et al., 2009; Hicks et al., 2014). 2DVM show a well-resolved Vp in both, north and south, segments. The Vp/Vs ratios show a less constrained area, mainly because of a lower number of S-phase onsets. For our 3DVM, Figure 3 shows a representative sample of the MRM (Figures S6 and S7 present the resolution obtained for all profiles in cross section and horizontal slices, respectively). From north to south, we observed how the central profiles are better resolved. At ~1°N, in profile 1, the lack of seismicity and data from OBS at this latitude confines the resolution contour to an area with data coming from a seismic cluster in the upper crust. In contrast, the rest of the profiles show wider resolution contours. In terms of MRM, the small SF and rounded shape of the resolution kernels indicate well-resolved areas. Although some areas in the marine forearc can show lateral smearing (P5–P6, see Figure S6), it is important to highlight how the resolved areas were increased trench-ward due to the presence of the OBS. The portion of the marine forearc devoid of OBSs (P1) is not resolved at shallow depths (<5–7 km). For Vp/Vs (Figure 3), the resolution contours are smaller due to the quality of S-phases detected, we were able to resolve the central part in all profiles. In terms of smearing, we see a transition in the shape of the resolution kernels that goes from small in the central part (around 0 km in the *x* axis) to a large-elongated shape near the edges, limiting the resolution in these areas (see Figure S6).

5.2. Checkerboard Test

Anomalies of 30 km width (Figures 4 and S8) show well recovered velocities (dv ~ 5%) down to ~40 km depth. Lateral and vertical extensions of the recovered anomalies show a recovery <2%. For smaller perturbations (15 km, Figure 4), areas of good recovery are similar to those from larger anomalies, showing

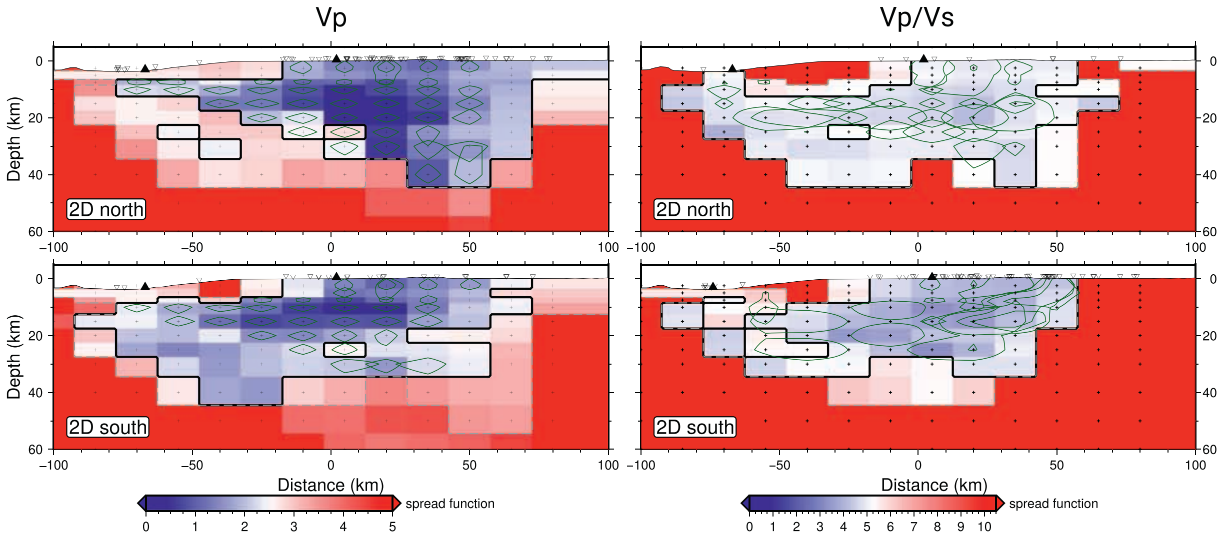

Figure 2. 2D model resolution matrix (MRM). Resolution contour estimation for the 2D Vp and Vp/Vs models in the north and south segments. Based on the MRM analysis, calculation of the spread function is displayed in a red/blue scale. Green lines show the 70% contour for the diagonal elements of the MRM. The distribution of the nodes in depth follows the layered structure derived in the minimum 1D model (León-Ríos et al., 2019; see Figure S2). In a W-E direction, node spacing is 15 km. Solid black triangles represent the projection of the trench (Collot et al., 2005) and coastline. Finally, inverted triangles are the stations projected on each profile in a region of ±12 km.

a reduction of recovered velocities (dv < 2%) when deeper than ~30 km. We observe a reduction in the recovering capacity in P1 where the lack of seismicity limits the resolution to a small region at shallower depths (<20 km) below the coastline. P2 shows a very good recovery reaching dv ~ 4% in its central region although the edges still show the effects of reduced seismicity. Profiles P4–P8 are completely recovered (dv ~ 5%) in the central areas, reaching good resolution up to the trench. Finally, the southernmost profile P10 also shows well recovered areas although the reduced seismicity in that region reduces the in-depth restoring capacity to <2% down to 20 km.

5.3. Synthetic Recovery Tests

The tests performed with synthetic travel times show a good recovery of different features included in each characteristic model. For the case of the near-trench low Vp anomalies centered at 5 km depth (Figures 4c and S9), we observe that P4 is more likely to recover the low Vp by getting values ~5 km/s down to 5 km depth. P5 restored the reduced velocities (~5.5 km/s) although the Vp = 5 km/s show only a small size down to 2.5 km depth. In terms of the low Vp anomaly at ~20 km depth in profile P7, the model can recover the anomaly although with a reduced amplitude.

5.4. Dependency on the 2D Starting Model: 2D-N and Merged 2D-N/2D-S

We explore the dependency of the solution on the starting model by testing two different initial models. In both cases, we followed the same procedure as for our actual model. For the case of the 2D-N characteristic model (see Figure S10), we inverted synthetic travel times calculated using the 2D-N model. We observe that the major features are recovered in almost all profiles, except in those with reduced seismicity correlating with areas which were already identified as regions of limited resolution. For the second test, we evaluate the dependency of the solution by merging the 2D-N and 2D-S models. To avoid a sharp velocity contrast at the interface of the two models, we interpolated the corresponding velocities to generate a smooth starting model. The merged model was subsequently inverted following the same workflow described for our staggered 3D modeling (see Figures S11 and S12). In general, Vp and Vp/Vs ratios derived using this merging approach show consistency with the results in our accepted solution. We observe that the main features at the surface and offshore are well resolved which reinforce the imaging capability of our data set. However,

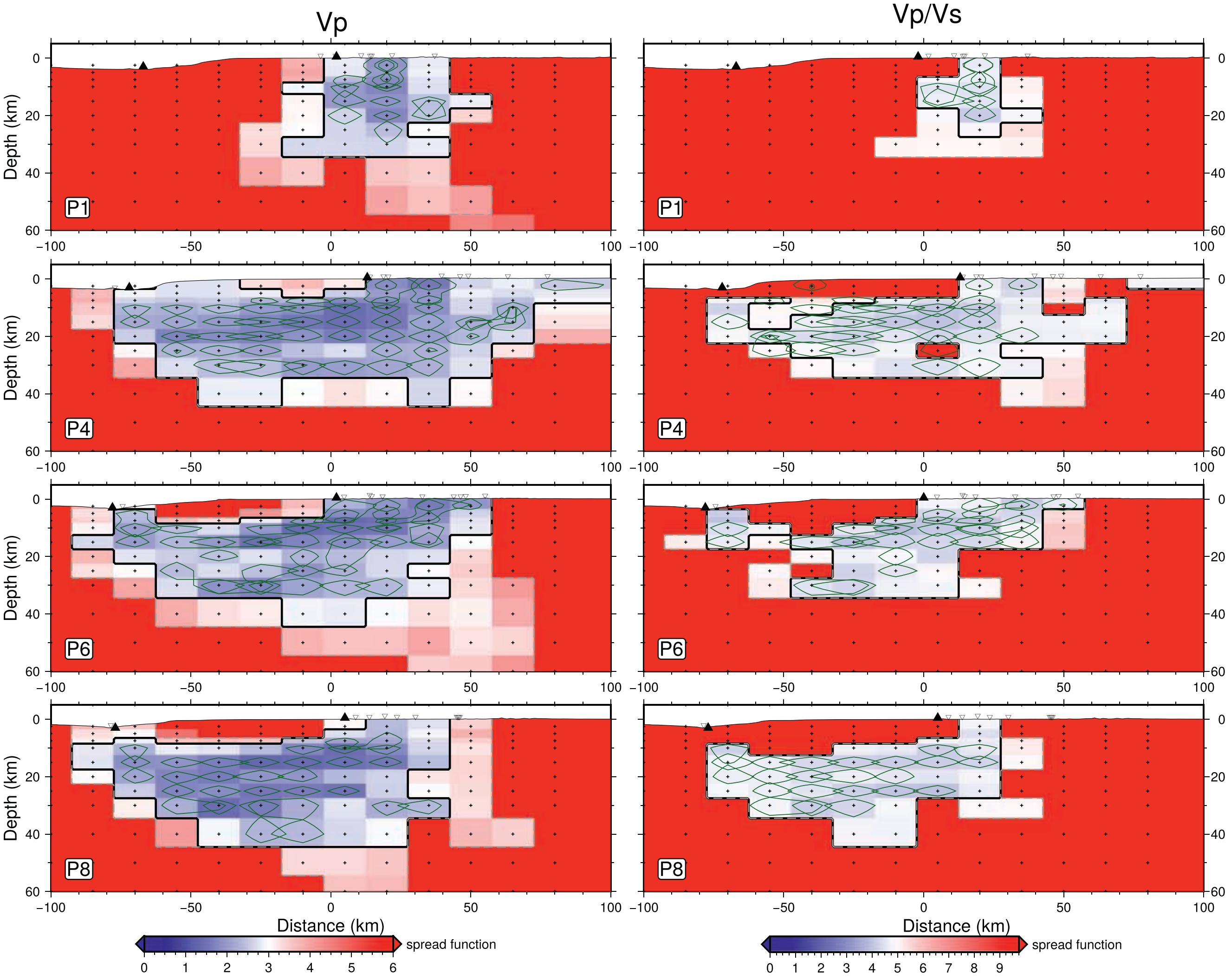

Figure 3. 3D model resolution matrix (MRM). Resolution contour estimation for the 3D Vp and Vp/Vs along representative profiles for the northern, central, and southern parts of the area of study. Based on the MRM analysis, calculation of the spread function is shown by a red/blue scale. Green lines show the 70% contour for the diagonal elements of the MRM. The distribution of the nodes in depth follow the layered structure derived in the minimum 1D model (León-Ríos et al., 2019; see Figure S2). In a W-E direction, node spacing is 15 km. Solid black triangles represent the projection of the trench (Collot et al., 2005) and coastline. Finally, inverted triangles are the stations projected on each profile in a region of ±12 km. See text for further information.

the along-strike smearing observed parallel to the trench suggests that this strategy can add artifacts to the solution in areas with reduced seismicity.

5.5. Finite Difference Ray Tracing

The synthetic test based on finite difference ray tracing, and therefore using a completely different approach of model representation and travel time calculation, suggests a robust model that it is capable to derive: first, the main 2D features starting from a minimum 1D model (Figure S13), and second, to recover the extent and amplitudes for both fast and slow anomalies offshore (Figure S14).

5.6. Bootstrap

For this test, we randomly created 100 subcatalogs comprised by 80% of the total events. These subsets of data were then inverted following the same inversion parameters as described for the 3DVM. We used the 100 resulting models to calculate the standard deviation at each node of the grid. In terms of velocity errors,

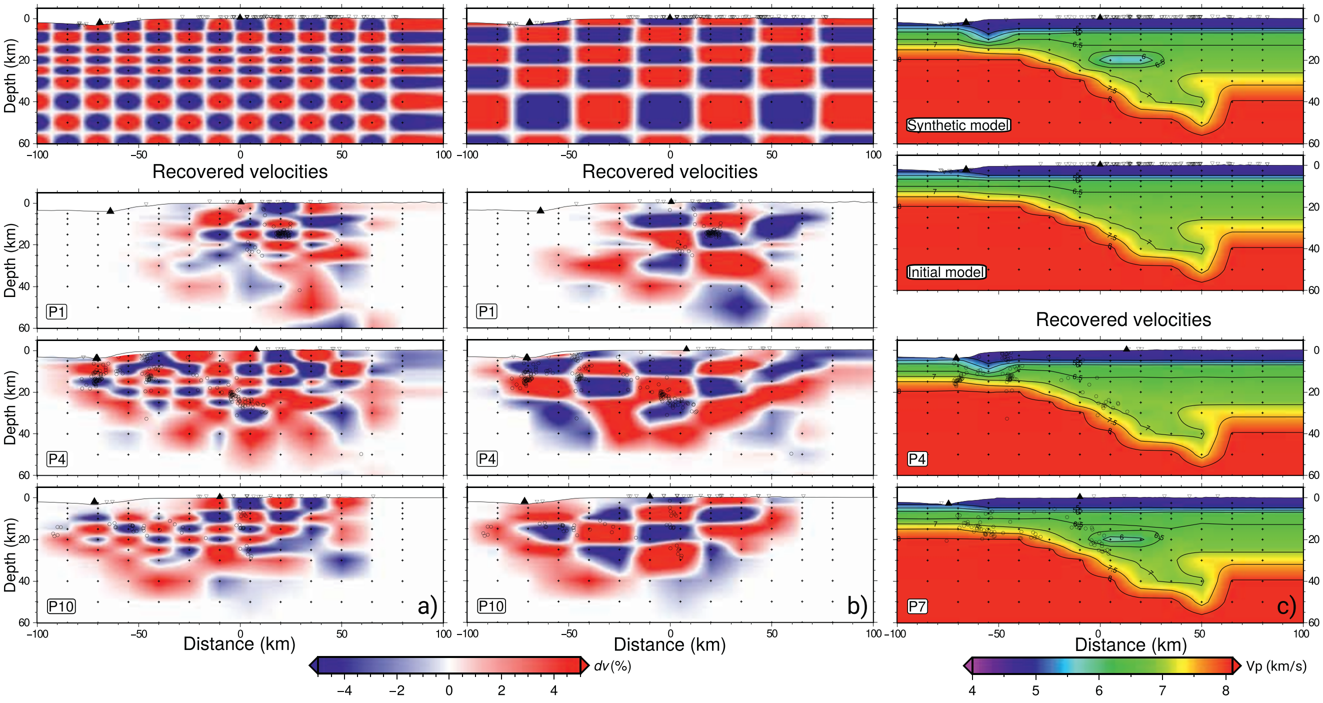

Figure 4. Synthetic recovery tests. Checkerboard test for (a) small, 15 km and (b) medium, 30 km anomalies. Top image show the input model comprised by alternated positive and negative anomalies of ±5% of the inverted model. Bottom images show the recovered velocities along representative profiles for the northern, central, and southern segments in our region of interest. (c) Restoring test for a seamount represented by low Vp (5.0 km/s) anomalies added in P4 and a low velocity anomaly (6.0 km/s) at 20 km depth in P7. Projection of the synthetic and initial model are shown at the top. The distribution of the nodes in depth follows the layered structure derived in the minimum 1D model (León-Ríos et al., 2019; see Figure S2). In a W-E direction, node spacing is 15 km. Solid black triangles represent the projection of the trench (Collot et al., 2005) and coastline. Finally, inverted triangles are the stations projected on each profile in a region of ±12 km. See Figures S4 and S5 for further details.

we consider the maximum values of the standard deviation and estimate uncertainties ~0.3 km/s for Vp and ~0.01 for Vp/Vs. The distribution of the standard deviation (Figure S15) is consistent with the well-resolved areas observed in the other tests. Finally, we combined the well-resolved areas from all the performed tests to derive the areas of good resolution highlighted in our accepted model in the following sections. In general, these areas extend ~130 km eastward from the trench axis and reach down to ~35 km in depth.

6. Results

The following sections describe the results shown in Figures 5–7. Cross sections were produced for 2DVM and 3DVM (see Figures 5 and 6, respectively). We used slab1.0 (Hayes et al., 2012) as a reference for the plate interface at depths greater than 15 km and modified the shallower part by using the trench location from Collot et al. (2005) and our obtained earthquake distribution. Also, horizontal slices for Vp and Vp/Vs were taken at 2, 5, 10, and 20 km depth to observe velocity changes in depth (Figure 7). The margin shows Vp/Vs ratios ranging from 1.74 to 1.94 in agreement with Hyndman (1979) and Christensen (1996, 2004) that suggested typical Vp/Vs values in the upper oceanic crust of 1.78–2.11 depending on the percentage of serpentine, fluids, or lithology.

6.1. Two-Dimensional Velocity Models

From the resulting 2DVM, we can identify first-order features in both, north and south, segments. Figure 5 shows cross sections for Vp and Vp/Vs where the Vp = 7.0 km/s contour images the geometry of the crustal part of the downgoing plate. We also observe elevated Vp/Vs ratios (~1.90) located close to the trench. In the overriding plate, velocity anomalies correspond to major geological structures, such as basins and geologic formations distributed along the margin. North and south profiles in Figure 5 show prominent low Vp

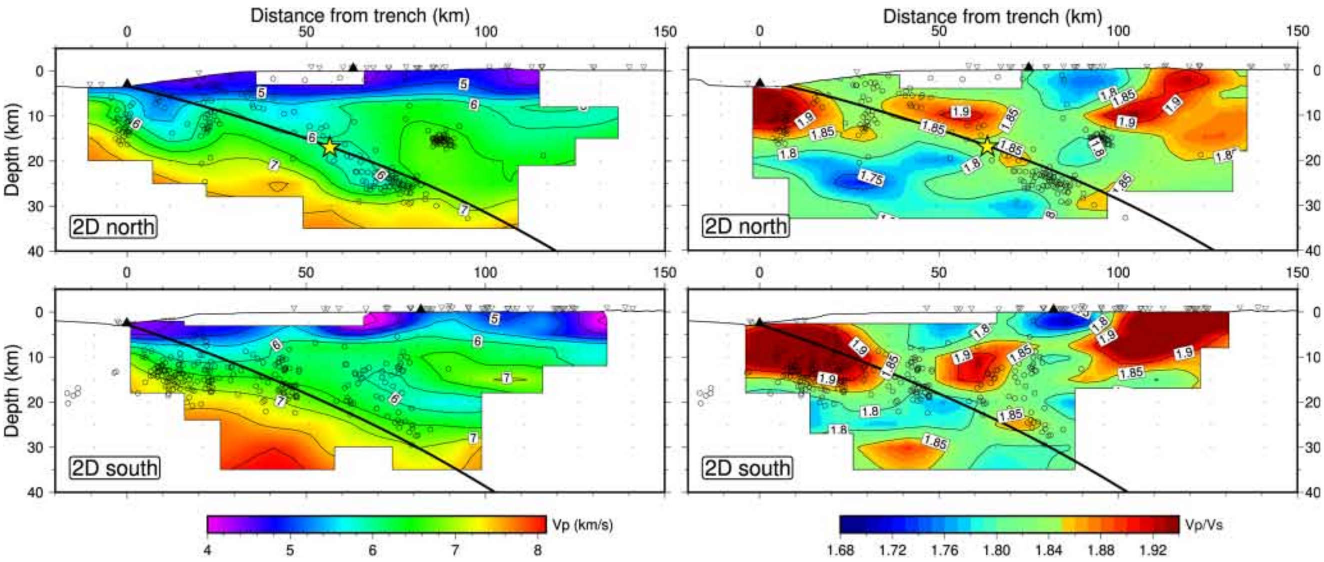

Figure 5. 2D velocity model. Two-dimensional models for both north (top) and south (bottom), Vp (left) and Vp/Vs (right). Velocities and Vp/Vs ratios are color coded and isocontours are plotted every 0.5 km/s and 0.05 for Vp and Vp/Vs, respectively. Well-resolved areas are highlighted based on the resolution tests. Relocated hypocenters are plotted in black circles and grid nodes are shown in black crosses. Yellow star in north, Vp and Vp/Vs, profiles indicates the epicenter for the 2016 Pedernales earthquake (Nocquet et al., 2017). The distribution of the nodes in depth follows the layered structure derived in the minimum 1D model (León-Ríos et al., 2019; see Figure S2). In a W-E direction, node spacing is 15 km. Solid black triangles represent the projection of the trench (Collot et al., 2005) and coastline. Inverted triangles are the stations projected on each profile in a region of ±12 km. Finally, the modified slab interface (see text for further details) is represented by solid black line.

anomalies (~4 km/s) and alternated distribution of Vp/Vs ratios, with low (~1.75) and high (~1.90) values, extending eastward at shallow depths. Geologic features associated with these anomalies have been mapped at the surface by Reyes and Michaud (2012) and will be discussed later. Finally, in terms of seismicity, we observe that most of the seismicity are located along the slab interface. However, we observe a change from a more interface-aligned organization of earthquakes in the north to a more dispersed distribution of events in the south.

6.2. Three-Dimensional Velocity Model

Figures 6 and 7 show our resulting Vp and Vp/Vs 3DVM together with the relocated seismicity, displayed in horizontal slices and cross sections, respectively. At shallow depths ($z = 2$ and 5 km, see Figure 6), we image a prominent elongated N-S feature (P, ~30 × 60 km) along the coastline, having Vp ranging from 5.0 km/s to Vp = 5.5 km/s. We also observe low velocities (M, Vp ~ 4.5 km/s) south and east of the high Vp anomaly, suggesting a high velocity contrast at shallow depth in the area. At the same depths ($z = 2$ and 5 km), high and low Vp/Vs ratio anomalies (>1.85 and <1.80) are observed at the location of the high (P) and low (M) Vp regions.

Cross sections in Figure 7 image in detail the uppermost part of the subducting oceanic Nazca plate. By comparing the depth of the Vp 7.2–7.5 km/s isocontour at ~20 km eastward of the trench, we observe a thick crust ~15 km which is consistent with previous observations for the Nazca plate thickness (Cano et al., 2014; Gailler et al., 2007; Sallarès & Charvis, 2003). In terms of Vp/Vs ratios, we find values ~1.90 close to the trench in profiles P2–P9 (Figure 7).

Close to the trench, a prominent low Vp anomaly (~5.5 km/s) is observed in the oceanic crust. Horizontal slices at $z = 10$ km, in Figure 6, show the along-strike extension where three low Vp patches (A1–A3) are illuminated. Moreover, a detailed inspection of the cross sections (see Figure 7), shows a prominent low Vp feature of ~20 km wide in P4. Also, this low Vp anomaly shows a broader extension to the south from P5 to P9. In terms of Vp/Vs, it is also possible to observe an N-S variation in the area where the low Vp anomaly is described. We image Vp/Vs ratios ~1.75 in P4–P5 that change to ~1.85 from P6 to P9 close to the trench.

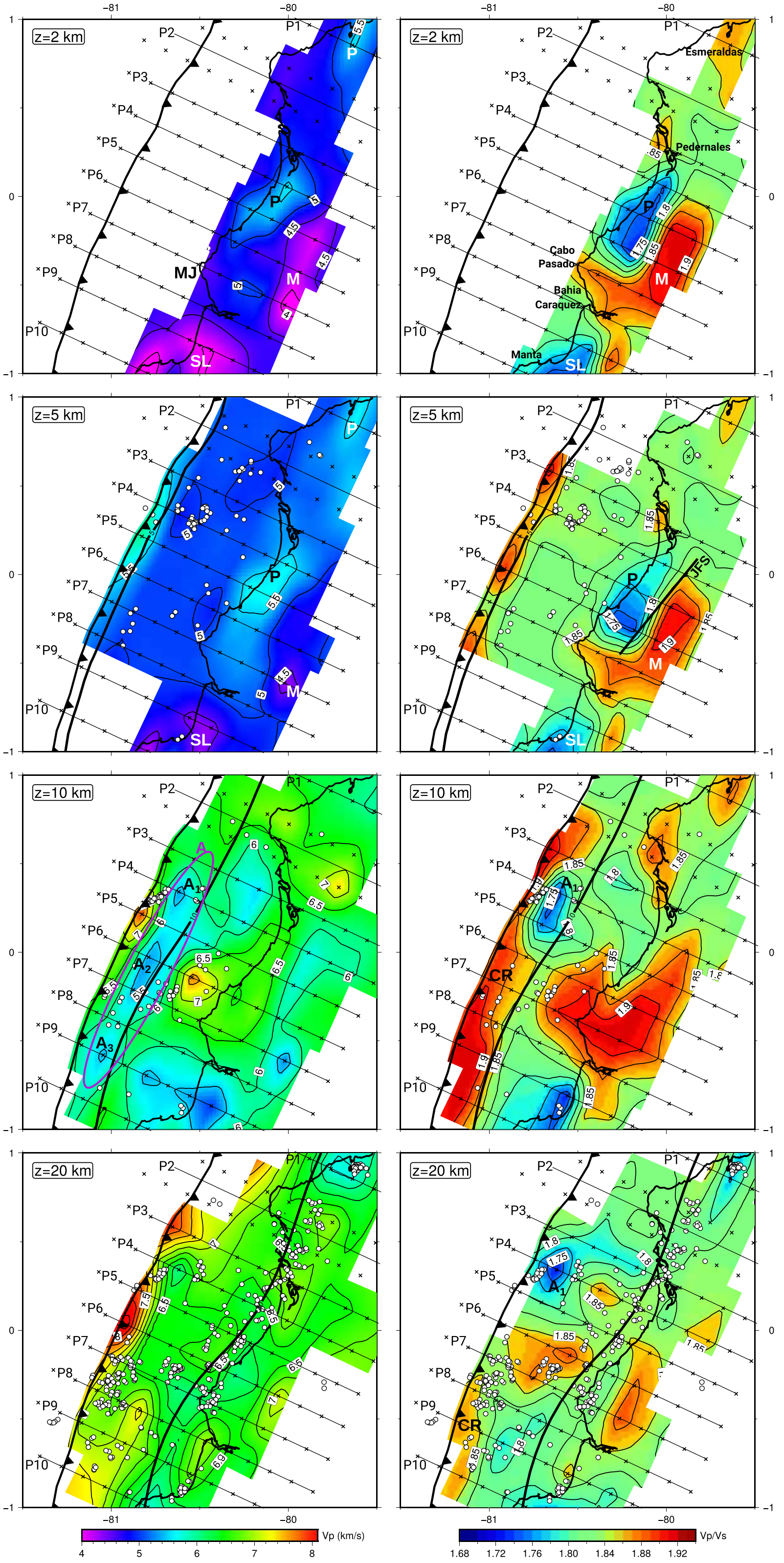
z=2 km
z=5 km
z=10 km
z=20 km
P1
P2
P3
P4
P5
P6
P7
P8
P9
P10
P
M
MJ
SL
Esmeraldas
Pedernales
Cabo Pasado
Bahia Caraquez
Manta
JFS
A1
A2
A3
CR
−81
−80
1
0
−1
Vp (km/s)
4
5
6
7
8
Vp/Vs
1.68
1.72
1.76
1.80
1.84
1.88
1.92

Finally, from the relocated data set displayed in vertical and horizontal profiles, we observed a clustered distribution mainly organized along the slab interface, as described by Agurto-Detzel et al. (2019), Meltzer et al. (2019), and Soto-Cordero et al. (2020) but also at shallower depths (<20 km) in the upper crust as discussed by León-Ríos et al. (2019) and Hoskins et al. (2020). Here, we provide a description of the seismicity distribution observed throughout the 3DVM.

A cluster of crustal seismicity seen in profile P1 occurred in July 2016 along the Esmeraldas segment. Cross sections in profiles P2–P5 show the seismicity mostly aligned along the slab interface at depths > 15 km. In contrast, close to the trench in P4, we observe a prominent subvertical organization of events showing a depth range between 5 and 10 km. Seismicity in profiles P6–P7 appears with a more disperse distribution. However, it is still possible to identify some clustering close to the trench (~10–15 km depth). P8 shows clustered activity in the oceanic crust, located ~10–15 km east from the trench. Finally, in profiles P9 and P10, the observed seismicity is reduced significantly with few events in the slab interface and also clustered activity in the upper crust with a vertical distribution occurring at shallower depths (~10–15 km) in P9.

7. Interpretation and Discussion

7.1. Upper Plate Crust

P wave velocities in the upper plate crust (UC) can be associated with geological structures described by Reyes and Michaud (2012) and shown in Figure 1b. Observations from horizontal slices at shallow depths ($z = 2$ and 5 km) are labeled in Figure 6 relating the high Vp (~5.5 km/s) feature to outcrops of the Piñon formation (P). The same structure is well imaged in Vp/Vs profiles P4–P6 in Figure 7. This formation is clearly imaged by relatively low Vp/Vs ratios (1.75–1.80) distributed along the coastline between 0.5°S and ~0.1°N, and it is part of the oceanic terranes in the overriding plate (Luzieux et al., 2006; Reyes & Michaud, 2012; Reynaud et al., 1999). We can estimate its lateral extent up to ~25 km. In contrast, at 2 km depth, we observed an elongated N-S orientated low Vp (M, ~4.5 km/s) body that extends southward. This feature can be associated with the northern part of a sedimentary basin, namely the Manabi basin (M; Reyes & Michaud, 2012). The Manabi basin is well identified by a large-scale (~80 × 27 km) NNE high Vp/Vs (1.85–1.90) anomaly associated with nonconsolidated and hydrated rocks. We also imaged what might be the basin depocenter by identifying a region of reduced Vp (4.5 km/s) and elevated Vp/Vs ratios (~1.85) down to 5 km depth (see Figure 6).

The Manabi basin is a large structure that extends for about 200 km along strike and its north-eastern boundary is controlled by the Jama Fault System (JFS) which separates this basin from the Cretaceous Piñon formation. The contrasted nature of these formations could be related to the high contrast imaged in the horizontal slices of both Vp and Vp/Vs models. This fact has been previously described based on station correction terms from our derived 1D velocity model (León-Ríos et al., 2019). Moreover, Vp/Vs cross sections P4–P6 (see Figure 7) highlighted this contrast of Vp/Vs ratios, around 100 eastward from the trench, up to 5–10 km depth. Collot et al. (2004) and Michaud et al. (2015) have suggested that the JFS extends offshore forming an active flower-like fault structure in the marine forearc; however, our model does not show clear evidence to support that hypothesis. Southernmost profiles P9 and P10 image reduced ratios covering a large area in the overriding plate. These anomalies can be associated with the San Lorenzo formation (SL) mapped by Reyes and Michaud (2012—Figure 6) and also observed by Lynner et al. (2020) and Koch et al. (2020).

Isovelocity contours of Vp ~ 6.0–6.2 km/s in cross sections (Figure 7) also contribute to imaging a transition zone in the marine forearc at depth above the interplate, which separates a wide deformed, eroded, and fractured trench-ward region of accreted oceanic Cretaceous rocks, with Vp ~ 5.5 km/s, from a

Figure 6. 3D velocity model, horizontal slices. Vp (left) and Vp/Vs (right) horizontal slices at 2, 5, 10, and 20 km depth. Velocities and Vp/Vs ratios are color coded and isocontours are plotted every 0.5 km/s and 0.05 for Vp and Vp/Vs, respectively. Well-resolved areas are highlighted based on the resolution tests. Velocity anomalies colocated to surface observations from Reyes and Michaud (2012) and cities referred in text are shown in $z = 2$ km. Profile and grid nodes locations are displayed by black solid line and crosses, respectively. Node spacing is 15 km for the W-E direction and 12 km for the N-S direction. Corresponding slab depth contour is represented by a thick black line. Seismicity is plotted by depth (d) following: $d \leq 5$ km in $z = 5$ km, $5 < d \leq 10$ km in $z = 10$ km, and $d > 10$ km in $z = 20$ km. P, Piñon outcrop; M, Manabi basin; MJ, Manta–Jama basin; SL, San Lorenzo block; JFS, Jama Fault System; CR, Carnegie Ridge; and A, A1–A3, anomalies described in text.

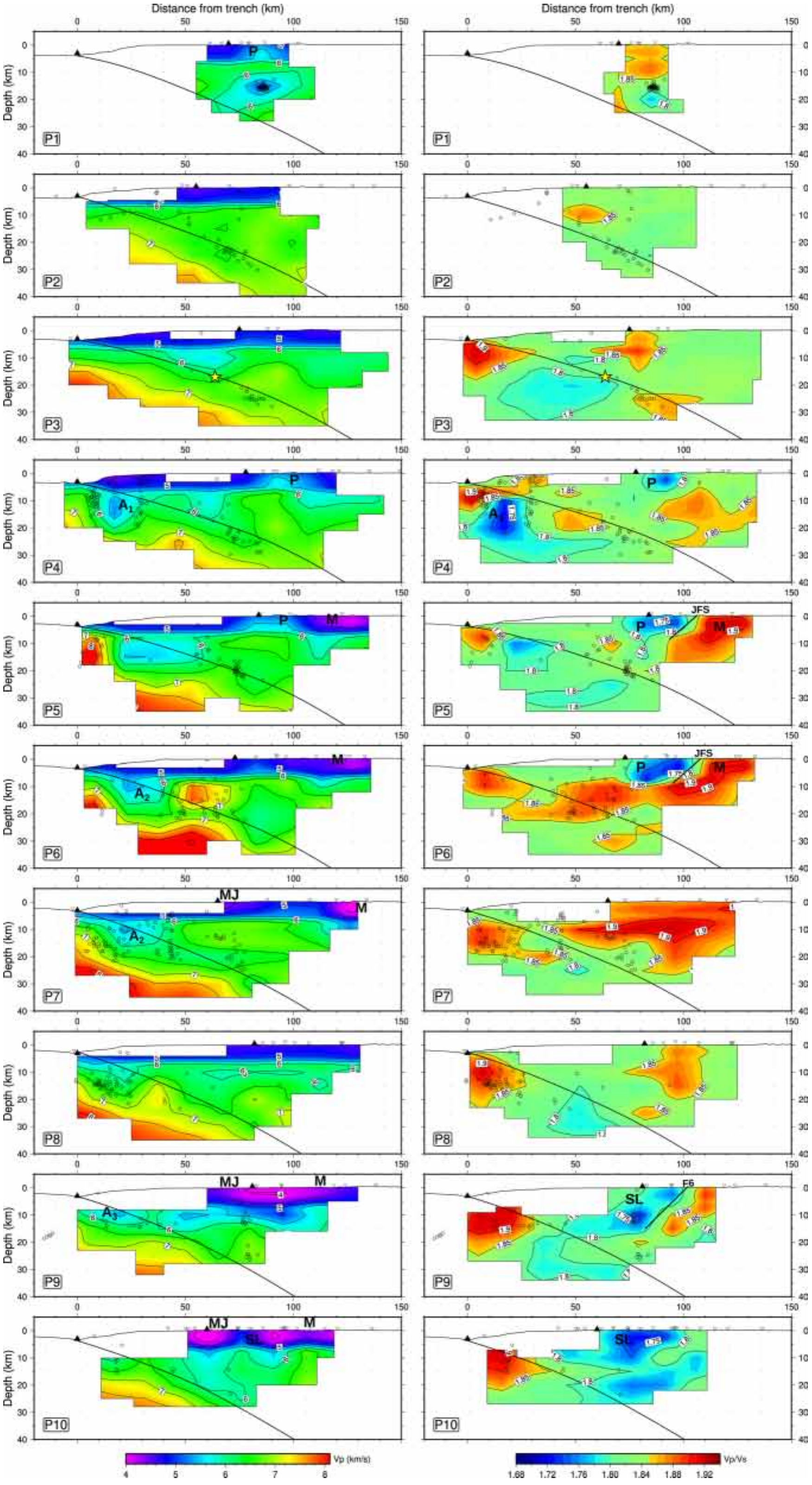
Distance from trench (km)
Distance from trench (km)
0
50
100
150
Depth (km)
0
10
20
30
40
P1
P2
P3
P4
P5
P6
P7
P8
P9
P10
P
A1
M
JFS
A2
MJ
A3
SL
F6
Vp (km/s)
4
5
6
7
8
Vp/Vs
1.68
1.72
1.76
1.80
1.84
1.88
1.92

deeper more consolidated, less deformed and more mechanically resistant area to the east (Vp > 6 km/s and depth > 7 km; Cano et al., 2014; Gailler et al., 2007). Following this isovelocity contour (Vp ~ 6.0–6.2 km/s) along the vertical sections (Figure 7), we observe that in profiles P3–P5, the transition zone is located between 50 and 60 km eastward of the trench and might be related to the west limit of the Piñon formation imaged at shallower depths by reduced Vp/Vs ratios (~1.75). As suggested by Wang and Bilek (2011) and Marcaillou et al. (2016), this possible highly damaged frontal zone can prevent seismic rupture to nucleate at shallow depths on the megathrust fault. The eastern limit of this frontal domain could indicate a major feature controlling the updip rupture extension of moderate-magnitude megathrust earthquakes such as the Mw 7.8 in 1942 and the Mw 7.8 in 2016 occurring on the deeper portion of the fault. Similar behavior has been proposed by Cano et al. (2014) for the northern Esmeraldas region and the Mw 7.7 earthquake in 1958 (see Figure 1a). As the ~50–60 km wide low velocity wedge is directly affected by the subducting plate and the possible frontal erosion caused by the incoming topography (Dominguez et al., 1998; Sage et al., 2006; von Huene et al., 2000), it is expected that the accreted volcanic rocks that shaped the oceanic terranes in the outermost forearc on this region are fluid-saturated, altered, and disaggregated (Cano et al., 2014; Contreras-Reyes et al., 2012; Marcaillou et al., 2016). Finally, toward southern profiles (P6–P8), the described transition zone reduces its extension to less than 40 km (at ~10 km depth) leading to a margin with Vp ~ 6 km/s, consistent with the observations made by Gailler et al. (2007).

7.2. Subducting Oceanic Lithosphere

In general, as it is shown in Figure 7, Vp velocities resulting from our 3DVM image a predominant area of Vp ~ 4.5–7.5 km/s dipping eastward that we associated with mid-oceanic ridge basalts and basaltic lavas formed at a spreading center that comprise the oceanic crust (White et al., 1992) but also to serpentinized rocks that contribute to reduce Vp values (Marcaillou et al., 2008). Because of the inherent limitations of our data set and model, with in-depth grid node spacing of 5 km (down to 30 km depth), we cannot assess an exact value for oceanic crustal thickness. Considering the isovelocity contour of 7.5 km/s that mimics the Moho, we have some insights on the downgoing plate characteristics. On average, we observe no significant changes in oceanic crustal thickness that appears to be around 15 km (see Figure S16). An abnormally thick oceanic crust has been previously observed by marine seismic experiments (Gailler et al., 2007; Sallarès & Charvis, 2003; Sallarès et al., 2005) in the area that is related to the presence of the Carnegie Ridge (previously identified as CR). Our tomography shows similar velocities for the upper crust from previous studies (Graindorge et al., 2004; Sallarès et al., 2005) and the presence of the CR is on all profiles where the base of the oceanic crust is resolved from P3 to P9, highlighting its extension under the margin. The CR resulted from the cooling of mantle melted material originated ~15–20 Myr B.P. by the interaction between the GHS and the Cocos-Nazca spreading center (Gailler et al., 2007; Lonsdale, 1978; Sallarès & Charvis, 2003), adding material to the lower layers of the oceanic crust and shifting the Moho location to greater depths (see $z = 20$ km in Figures 6 and 7). Furthermore, looking at the along-strike variations of the 7.5 km/s isovelocity contour on profiles P4–P7 (see Figure S16), the flattening of the contour at ~40 km from the trench shows a thinning of the downgoing crust that could be interpreted as the eastern border of the CR or strong variations of the CR structure (see Figure 8). If indeed we observe the eastern border of the CR, it seems to be close to the coast, not having reached it yet. This position of the eastern border of the CR is consistent with the extension of the Malpelo ridge, as both were part of the same ridge (Lonsdale, 1978). Such interpretation implies a prior process that resulted in the coastal Cordillera uplift such as stripping events at the base of the forearc crust (Ménant et al., 2020) and/or deep slab folding at depth (Cerpa et al., 2015).

Figure 7. 3D velocity model, cross sections. Three-dimensional models for both Vp (left) and Vp/Vs (right) based on the inversion of a smooth initial 2D initial model and the refined arrival times calculated in the 2D-N and 2D-S inversions. Results are shown along 10 W-E profiles. Vp velocities and Vp/Vs ratios are color coded and isocontours are plotted every 0.5 km/s and 0.05 for Vp and Vp/Vs, respectively. Well-resolved areas are highlighted based on the resolution tests. Location of profiles, P1–P10, is shown in Figure 1. Width for projection of hypocenters and stations is 22 km. Relocated hypocenters are plotted in black circles, and stations are represented by inverted triangles. Grid nodes are displayed in black crosses and solid black triangles represent the projection of the trench and coastline. Yellow star in P3 indicates the hypocenter for the 2016 Pedernales earthquake (Nocquet et al., 2017). Modified slab interface (see text for further details) is represented by solid black line. P, Piñon outcrop; M, Manabi basin; MJ, Manta–Jama basin; SL, San Lorenzo block; JFS, Jama Fault System; CR, Carnegie Ridge; F6, El Aromo fault; A, A1–A3, anomalies described in text.

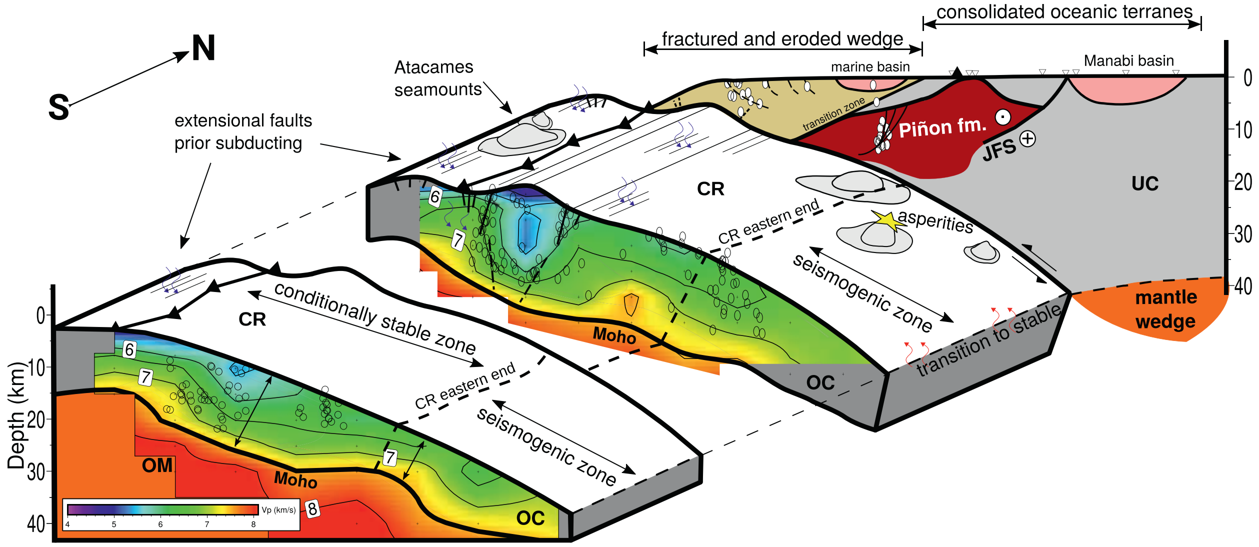

Figure 8. Interpretative sketch. Structural synthesis based on the main findings of this work around profiles P4 and P7. UC, upper plate crust; OC, oceanic crust; OM, oceanic mantle; CR, Carnegie Ridge; JFS, Jama Fault System, with strike-slip displacement indicated by the dot and cross. Vp velocities at P4 and P7 are projected in cross sections. Hypocenters are shown in circles. Black triangles represent the trench axis and the coastline. Inverted triangles indicate station locations. Yellow star represents the epicenter of the 2016 Pedernales earthquake (Nocquet et al., 2017). Arrows in the front panel indicate the thickness of the OC. We observe a thinning of the OC at depths ~20–30 km which we interpret as the eastern end of the CR. Vertical scale exaggeration 1:1.5.

In terms of Vp/Vs, we image elevated ratios of $\sim$1.85 dipping eastward, close to the trench. This feature is intersected with Vp/Vs ratios $\sim$1.80 related to the oceanic terranes (see profiles P3–P5 in Figure 7). We observe differences in the Vp/Vs ratios between north (P2–P5) and south (P6–P10) segments along the downgoing plate. The CR shows high Vp/Vs ratio anomaly ($>$1.85) that changes to normal oceanic values when the slab reaches 10 km depth (P6–P10), associated with seismicity on P7–P9. To the north this feature seems affected by the low Vp anomaly observed on P3 and P5 and shows a low Vp/Vs value.

7.3. Elevated Vp/Vs Close to the Trench

Our 2DVM (see Figure 5) shows for the north and south segments elevated Vp/Vs ratio contours ($>$1.85), illuminating the subducting oceanic crust close to the trench. However, both profiles reach values $>$1.90 indicating a highly hydrated region close to the trench (Hacker et al., 2003). More in detail, the 3DVM helps us to identify the areas where these highs in Vp/Vs ratio are located. Horizontal slices, at $z = 5$ km, in Figure 6, show two small patches of Vp/Vs $\sim$ 1.85 located at 0° and 0.5°N. Similarly, slice at $z = 10$ km images two N-S elongated anomalies of elevated ratios ($>$1.85) that extend for $\sim$50 km, in the north, and $\sim$100 km in the south, respectively. High Vp/Vs ratios along the trench axis have been observed along other subduction zones (e.g., northeastern Japan [Nakajima et al., 2001], central Chile [Haberland et al., 2009; Hicks et al., 2014], and Costa Rica [Bangs et al., 2015]). This feature is associated with the lithology of the oceanic crust, the presence of fluids from dehydrating subducted sediments (Husen et al., 2000), and a hydrated oceanic crust with extensional faults formed before subduction in the outer rise (von Huene, Ranero, & Vannucchi, 2004a; von Huene, Ranero, & Watts, 2004b).

The central Ecuadorian subduction zone has been described as an erosive margin with a low input of sediments (Collot et al., 2002; Gailler et al., 2007; Marcaillou et al., 2016), and therefore other mechanisms explaining the elevated Vp/Vs along the trench are needed. Cross sections P4–P5, in Figure 7, suggest a positive relation between subducting topography and elevated Vp/Vs ratios ($>$1.85) on the edges of these features. Moreover, the seismicity distributed with a subvertically disposition of $\sim$10 km length inside the oceanic crust gives us insights about possible deformed and fractured areas caused either by the collision of bathymetric features with the overriding plate and/or the reactivation of extensional faults on the Nazca plate, created by the outer rise bending prior subducting (von Huene & Culotta, 1989; von Huene, Ranero, & Vannucchi, 2004a; von Huene, Ranero, & Watts, 2004b). In Figure 8, we suggest that the high ratios imaged by our Vp/Vs model are also associated with the subduction of bathymetric features, such as the Atacames seamounts, which cause deformation and generation of weakness areas close to the trench. This process contributes to high rates of fluids migration by increasing the porosity and permeability on both plates involved. On the other hand, the broader extent of elevated Vp/Vs ratios >1.85 in the southern segment (P6–P10) are mainly related to the presence of the CR and its sharp topography (Figure S17). This bathymetric feature and the previously mentioned outer rise bending contribute to a pervasively fractured and highly hydrated oceanic crust.

7.4. Low Velocities in the Oceanic Crust

Our 3DVM illuminates a highly heterogeneous margin which is largely affected by the presence of topographic features on the seafloor. Horizontal slices at $z = 10$ km (see Figure 6) show a prominent elongated N-S feature (A) with Vp ~ 5.5 km/s located ~10 km eastward of the trench axis. Restoring and resolution tests in Supplementary Figures 5–8 support the robustness of this intriguing feature. Moreover, the inspection of the MRM along strike (Figure S6) show small SF and rounded 70% contour lines indicating a reduced along-strike “smearing” and therefore a well-resolved area. The along-strike length of this anomaly (~130 km) is consistent with the incoming bathymetric structures in the area (see Figure S17). Moreover, lower Vp (~5.0 km/s) anomalies are confined to smaller areas in P4, P6-P7 and P9. These observations can be complemented by collocating the observed Vp to the imaged Vp/Vs ratios. Horizontal slices in Figure 6 allow us to estimate the dimension of the observed features by imaging a rounded, ~15 × 25 km2 (at $z = 10$ km), low Vp/Vs ratios anomalies (~1.75), located around P4.

Cross sections in Figure 7 help us to discuss the in-depth extension of the observed anomalies. Here, we focus on P4 which shows a prominent low Vp body (A1, ~5.0–5.5 km/s) at ~20 km from the trench that it is flanked by two areas with Vp ~ 6.0 km/s on the sides. This feature agrees in shape and location with the observations described by Marcaillou et al. (2016) who estimated a ~2.5-km high seamount through an active seismic experiment. It also matches with the residual bathymetry derived by Agurto-Detzel et al. (2019—see Figure S17). Therefore, we interpret the observed low Vp anomaly as a seamount coming from the Atacames seamount chain, in the northern edge of the CR, (P4, Vp ~ 5.0 km/s) surrounded by Vp ~ 5.5 km/s that could be related to possible thermal anomalies associated with the origin of these structures and/or possible serpentinization as observed farther north by Marcaillou et al. (2008). The seismicity distribution also contributes to reinforce our interpretation. In P4 (see Figure 7), we observe two vertical clusters of events suggesting that the flanks of the seamount are under a high stress regime promoting faulting and seismic stress release. The clustered seismicity allows us to estimate a ~15–20 km lateral extension of this feature.

In relation to the origin of the observed low velocities, studies in young seamounts have shown that it is possible to observe low Vp in its structure (e.g., Caplan-Auerbach & Duennebier, 2001; Kopp et al., 2004). In the case of the Ecuadorian margin, it has been estimated that the Atacames seamounts were created around ~20–15 Myr ago in the GHS (Lonsdale, 1978; Sallarès & Charvis, 2003) which fits the young age hypothesis. Moreover, the erosive margin might have contributed to increasing the pressure along the seamount axis creating weaker areas in its base leading to the observed reduced velocities.

Further south, the relation between low Vp (~5.5 km/s) and high Vp/Vs (>1.85) suggests a different interpretation for this segment. Between P6 and P8, we observe a broader low Vp (A2–A3, ~5.5 km/s) anomaly that might correspond to material of the CR. Moreover, the elevated Vp/Vs ratios (~1.85) imaged along P6–P10 might point to a deeply fractured and highly hydrated incoming CR.

7.5. Structures Controlling the Seismicity

Figures 6 and 7 show the distribution of the seismicity over both Vp and Vp/Vs 3DVM. Although most of the relocated data sets are distributed along the plate interface, we identified several clusters of seismicity that can be related to structural features imaged by our 3DVM.

As we mentioned before, in the subducting Nazca plate, between latitudes ~1°N and ~2°S, the Atacames seamounts and the CR contribute to increase deformation and therefore to creating and/or reactivating extensional faults in the Nazca plate. This process, plus the bending of the plate prior subducting that causes extensional faulting, facilitates the occurrence of clustered seismicity along small-scale faults in the oceanic crust (see Figure 8). In the case of the Atacames seamounts, its influence on the Ecuadorian margin can be observed in the bathymetry of the marine forearc (Barnes et al., 2010; Collot et al., 2005; Marcaillou et al., 2016; von Huene, Ranero, & Vannucchi, 2004a; von Huene, Ranero, & Watts, 2004b) and also inferred by the seismicity detected at shallow depths in the marine eroded wedge suggesting a highly fractured region. Subducted seamounts can also act as asperities/barriers at greater depths (>15 km) contributing to the nucleation and/or cessation of intermediate-magnitude (M 7.5–8.0, Bilek et al., 2003) megathrust earthquakes (Wang & Bilek, 2011; Watts et al., 2010).

The CR seems to be the main feature controlling the seismicity in the margin between P3 and P10. Several studies have suggested that ridges may act aseismically and/or promote creep on the megathrust fault accompanied with small events (e.g., Wang & Bilek, 2011). For the CR, Gutscher et al. (1999) described how large earthquakes have not ruptured across this feature. Graindorge et al. (2004) suggested a greater period of recurrence of large earthquakes in that region in comparison with the northern segment. Recently, Agurto-Detzel et al. (2019) also proposed differences on the slip behavior for North and South segments. Based on the imaged Vp and Vp/Vs models, we suggest that this large-scale marine feature might contribute to a deeply fractured and highly hydrated oceanic crust promoting the circulation of fluids to greater depths (~20–30 km). Fluids would change the local behavior on the slab interface from unstable slip to conditionally stable (Kodaira et al., 2004) and therefore impede the occurrence of large megathrust earthquakes. These conditionally stable parts seem also to be favorable for SSE (e.g., Tokai segment in Nankai trench) and has been described in the area by Rolandone et al. (2018).

In the upper crust, several small- to large-scale faults might have been activated after the 2016 Pedernales earthquake. The shallow clustered seismicity observed close to the Esmeraldas segment (~1°N, P1) is related to crustal extension (Agurto-Detzel et al., 2019; Hoskins et al., 2020) and can be associated with the activation of the Tanigüe fault (Michaud et al., 2015—see F11 in Figure 1b) which may extend down to ~15 km reaching a low Vp/Vs rounded-like body (~1.80) capable to produce this type of confined earthquakes. To the south (~1°S), we observe clustered vertically aligned seismicity, at ~10–15 km depth, in the southernmost profile P9. Figure 1b helps us to relate these events with the surface projection of the El Aromo fault (F6) which has been previously described as an active structure by Segovia et al. (2018) and it is well imaged in our Vp/Vs model by a strong contrast between elevated and reduced ratios (Figure 7).

8. Conclusion

Using the unprecedented rapid deployment that recorded the regular seismic activity together with the aftershock sequence unfolded by the 2016 Pedernales earthquake, we built a high-quality data set of manually picked P- and S-phases, which were used to derive a 3DVM for Vp velocities and Vp/Vs ratios. We imaged the seismotectonic and geological velocity structure of the central Ecuadorian subduction zone. Velocities (~4.5–7.5 km/s) in the downgoing plate highlight the roughness of the incoming oceanic crust. Moreover, the observed Vp/Vs anomalies ranging from 1.74 to 1.95 suggest a heterogeneous and hydrated margin. We imaged the subduction of long-scale bathymetric features, such as the Atacames seamounts and the CR, which seems to contribute to the high circulation of fluids, especially close to the trench.

These features also play an important role in controlling the seismic behavior of the margin. We identified a subducting seamount, from the Atacames chain, with reduced Vp velocities (~5.0 km/s) and Vp/Vs ratios (1.75) associated with features with young magmatic material. On the other hand, the CR seems to be the main feature controlling the seismicity in the region, by promoting creeping and SSE caused by fluids migrating from a deeply fractured and highly hydrated oceanic crust. This fact is directly linked to the updip rupture limit of large megathrust earthquakes in the northern segment and the absence of large megathrust earthquakes in the southern region over the instrumental period.

Finally, our observations show the relevance of having well-resolved Vp and Vp/Vs models that complement each other in order to give a full interpretation, especially in highly heterogeneous and segmented regions such as the Ecuadorian margin.

Data Availability Statement

Data available at IRIS website http://www.iris.edu/dms/nodes/dmc/ using the network code 8G (Meltzer & Beck, 2016), EC (Alvarado et al., 2018) and G (Institut de Physique du Globe de Paris & Ecole et Observatoire des Sciences de la Terre de Strasbourg, 1982). Data from the emergency deployment XE available through Regnier et al. (2016). Earthquakes catalog is available through Agurto-Detzel et al., 2019. Model data are available in the KIT open repository doi:10.5445/IR/1000126350.

Acknowledgments
This study was supported by IGEPN, IRD, the INSU-CNRS, and the ANR grant REMAKE ANR-15-CE04-0004. The UK portion of the temporary deployment was supported by NERC grant NE/P008828/1. The US portion of the temporary deployment was supported by IRIS PASSCAL and NSF RAPID Program Award EAR-1642498. S.L.-R. acknowledges partial support from ANID under Programa Formación de Capital Humano Avanzado, Becas Chile (grant 8068/2015). H.A.-D. acknowledges support from ANR project ANR-15-CE04-0004 and UCA/JEDI project ANR-15-IDEX-01. We are also indebted to the people at Geoazur laboratories and INOCAR by its contribution in the installation of OBSs at sea in very harsh environments. Also we extend the acknowledgment to the staff at IGEPN for the continuous support during the deployment and service of the inland stations. Finally, the authors want to thank all the people in Ecuador who allowed us to install our stations in their houses, big thanks for your hospitality, patience, and help when it was needed.

References

Abe, K. (1979). Size of great earthquakes of 1837–1974 inferred from tsunami data. *Journal of Geophysical Research*, *84*(B4), 1561–1568.

Agudelo, W., Ribodetti, A., Collot, J. Y., & Operto, S. (2009). Joint inversion of multichannel seismic reflection and wide-angle seismic data: Improved imaging and refined velocity model of the crustal structure of the North Ecuador–South Colombia convergent margin. *Journal of Geophysical Research*, *114*, B02306. https://doi.org/10.1029/2008JB005690

Agurto, H., Rietbrock, A., Barrientos, S., Bataille, K., & Legrand, D. (2012). Seismo-tectonic structure of the Aysén Region, Southern Chile, inferred from the 2007 Mw = 6.2 Aysén earthquake sequence. *Geophysical Journal International*, *190*(1), 116–130.

Agurto-Detzel, H., Font, Y., Charvis, P., Rietbrock, A., Ambrois, D., Paullato, M., et al. (2019). Ridge subduction and afterslip control aftershock distribution of the 2016 Mw 7.8 Ecuador earthquake. *Earth and Planetary Science Letters*, *520*, 63–76.

Alvarado, A., Audin, L., Nocquet, J. M., Jaillard, E., Mothes, P., Jarrín, P., et al. (2016). Partitioning of oblique convergence in the Northern Andes subduction zone: Migration history and the present-day boundary of the North Andean Sliver in Ecuador. *Tectonics*, *35*, 1048–1065. https://doi.org/10.1002/2016TC004117

Alvarado, A., Ruiz, M., Mothes, P., Yepes, H., Segovia, M., Vaca, M., et al. (2018). Seismic, volcanic, and geodetic networks in Ecuador: Building capacity for monitoring and research. *Seismological Research Letters*, *89*(2A), 432–439.

Araujo, S. (2016). *Tomographie de la croûte et du manteau Équatoriens à partir des données du réseau sismologique national. Geophysics [physics.geo-ph]*. France: Université Grenoble Alpes. https://hal.inria.fr/tel-01530749/

Bangs, N. L., McIntosh, K. D., Silver, E. A., Kluesner, J. W., & Ranero, C. R. (2015). Fluid accumulation along the Costa Rica subduction thrust and development of the seismogenic zone. *Journal of Geophysical Research: Solid Earth*, *120*, 67–86. https://doi.org/10.1002/2014JB011265

Barnes, P. M., Lamarche, G., Bialas, J., Henrys, S., Pecher, I., Netzeband, G. L., et al. (2010). Tectonic and geological framework for gas hydrates and cold seeps on the Hikurangi subduction margin, New Zealand. *Marine Geology*, *272*(1–4), 26–48.

Beck, S. L., & Ruff, L. J. (1984). The rupture process of the great 1979 Colombia earthquake: Evidence for the asperity model. *Journal of Geophysical Research*, *89*(B11), 9281–9291.

Bilek, S. L. (2010). Invited review paper: Seismicity along the South American subduction zone: Review of large earthquakes, tsunamis, and subduction zone complexity. *Tectonophysics*, *495*(1–2), 2–14.

Bilek, S. L., Schwartz, S. Y., & DeShon, H. R. (2003). Control of seafloor roughness on earthquake rupture behavior. *Geology*, *31*(5), 455–458.

Calahorrano, A., Sallarès, V., Collot, J. Y., Sage, F., & Ranero, C. R. (2008). Nonlinear variations of the physical properties along the southern Ecuador subduction channel: Results from depth-migrated seismic data. *Earth and Planetary Science Letters*, *267*(3–4), 453–467.

Cano, L. C. G., Galve, A., Charvis, P., & Marcaillou, B. (2014). Three-dimensional velocity structure of the outer fore arc of the Colombia-Ecuador subduction zone and implications for the 1958 megathrust earthquake rupture zone. *Journal of Geophysical Research: Solid Earth*, *119*(2), 1041–1060. http://dx.doi.org/10.1002/2012jb009978

Caplan-Auerbach, J., & Duennebier, F. K. (2001). Seismicity and velocity structure of Loihi Seamount from the 1996 earthquake swarm. *Bulletin of the Seismological Society of America*, *91*(2), 178–190.

Cerpa, N. G., Araya, R., Gerbault, M., & Hassani, R. (2015). Relationship between slab dip and topography segmentation in an oblique subduction zone: Insights from numerical modeling. *Geophysical Research Letters*, *42*, 5786–5795. https://doi.org/10.1002/2015GL064047

Chlieh, M., Mothes, P. A., Nocquet, J. M., Jarrin, P., Charvis, P., Cisneros, D., et al. (2014). Distribution of discrete seismic asperities and aseismic slip along the Ecuadorian megathrust. *Earth and Planetary Science Letters*, *400*, 292–301.

Christensen, N. I. (1996). Poisson's ratio and crustal seismology. *Journal of Geophysical Research*, *101*(B2), 3139–3156.

Christensen, N. I. (2004). Serpentinites, peridotites, and seismology. *International Geology Review*, *46*(9), 795–816.

Collings, R., Lange, D., Rietbrock, A., Tilmann, F., Natawidjaja, D., Suwargadi, B., et al. (2012). Structure and seismogenic properties of the Mentawai segment of the Sumatra subduction zone revealed by local earthquake traveltime tomography. *Journal of Geophysical Research*, *117*, B01312. https://doi.org/10.1029/2011JB008469

Collot, J. Y., Charvis, P., Gutscher, M. A., & Operto, S. (2002). Exploring the Ecuador–Colombia active margin and interplate seismogenic zone. *EOS, Transactions American Geophysical Union*, *83*(17), 185–190.

Collot, J. Y., Marcaillou, B., Sage, F., Michaud, F., Agudelo, W., Charvis, P., et al. (2004). Are rupture zone limits of great subduction earthquakes controlled by upper plate structures? Evidence from multichannel seismic reflection data acquired across the northern Ecuador–southwest Colombia margin. *Journal of Geophysical Research*, *109*, B11103. https://doi.org/10.1029/2004JB003060

Collot, J. Y., Migeon, S., Spence, G., Legonidec, Y., Marcaillou, B., Schneider, J. L., et al. (2005). Seafloor margin map helps in understanding subduction earthquakes. *Eos, Transactions American Geophysical Union*, *86*(46), 463–465.

Collot, J. Y., Sanclemente, E., Nocquet, J. M., Leprêtre, A., Ribodetti, A., Jarrin, P., et al. (2017). Subducted oceanic relief locks the shallow megathrust in central Ecuador. *Journal of Geophysical Research: Solid Earth*, *122*, 3286–3305. https://doi.org/10.1002/2016JB013849

Contreras-Reyes, E., Jara, J., Grevemeyer, I., Ruiz, S., & Carrizo, D. (2012). Abrupt change in the dip of the subducting plate beneath north Chile. *Nature Geoscience*, *5*(5), 342–345.

Dominguez, S., Lallemand, S. E., Malavieille, J., & von Huene, R. (1998). Upper plate deformation associated with seamount subduction. *Tectonophysics*, *293*(3–4), 207–224.

Dorbath, L., Cisternas, A., & Dorbath, C. (1990). Assessment of the size of large and great historical earthquakes in Peru. *Bulletin of the Seismological Society of America*, *80*(3), 551–576.

Eberhart-Phillips, D. (1986). Three-dimensional velocity structure in northern California Coast Ranges from inversion of local earthquake arrival times. *Bulletin of the Seismological Society of America*, *76*(4), 1025–1052.

Eberhart-Phillips, D. (1990). Three-dimensional *P* and *S* velocity structure in the Coalinga region, California. *Journal of Geophysical Research*, *95*(B10), 15343–15363.

Eberhart-Phillips, D. (1993). Local earthquake tomography: Earthquake source regions. *Seismic Tomography: Theory and Practice*.

Eberhart-Phillips, D., & Michael, A. J. (1998). Seismotectonics of the Loma Prieta, California, region determined from three-dimensional V p, V p/V s, and seismicity. *Journal of Geophysical Research: Solid Earth*, *103*(B9), 21099–21120.

Egred, J. (1968). Breve historia sísmica de la República del Ecuador (1534–1965). *Boletín Bibliográfico de Geofisica y Oceanografía Americanas*, vol. *4*, 2a edicion (147–158).

Evans, J. R., & Achauer, U. (1993). Teleseismic velocity tomography using the ACH method: Theory and application to continental-scale studies. In H. M. Iyer, & K. Hirahara (Eds.), *Seismic tomography: Theory and practice* (pp. 319–360). London, UK: Chapman & Hall.

Evans, J. R., Eberhart-Phillips, D., & Thurber, C. H. (1994). User's manual for SIMULPS12 for imaging Vp and Vp/Vs: A derivative of the "Thurber" tomographic inversion SIMUL3 for local earthquakes and explosions. *U.S. Geological Survey Open-File Report*, 94–431.

Font, Y., Segovia, M., Vaca, S., & Theunissen, T. (2013). Seismicity patterns along the Ecuadorian subduction zone: New constraints from earthquake location in a 3-D a priori velocity model. *Geophysical Journal International*, *193*(1), 263–286.

Gailler, A., Charvis, P., & Flueh, E. R. (2007). Segmentation of the Nazca and South American plates along the Ecuador subduction zone from wide angle seismic profiles. *Earth and Planetary Science Letters*, *260*(3–4), 444–464.

Garcia-Cano, L. C. G., Galve, A., Charvis, P., & Marcaillou, B. (2014). Three-dimensional velocity structure of the outer fore arc of the Colombia–Ecuador subduction zone and implications for the 1958 megathrust earthquake rupture zone. *Journal of Geophysical Research: Solid Earth*, *119*, 1041–1060. https://doi.org/10.1002/2012JB009978

Graindorge, D., Calahorrano, A., Charvis, P., Collot, J. Y., & Bethoux, N. (2004). Deep structures of the Ecuador convergent margin and the Carnegie Ridge, possible consequence on great earthquakes recurrence interval. *Geophysical Research Letters*, *31*, L04603. https://doi.org/10.1029/2003GL018803

Gutscher, M. A., Malavieille, J., Lallemand, S., & Collot, J. Y. (1999). Tectonic segmentation of the North Andean margin: Impact of the Carnegie Ridge collision. *Earth and Planetary Science Letters*, *168*(3–4), 255–270.

Haberland, C., Rietbrock, A., Lange, D., Bataille, K., & Dahm, T. (2009). Structure of the seismogenic zone of the southcentral Chilean margin revealed by local earthquake traveltime tomography. *Journal of Geophysical Research: Solid Earth*, *114*(B1).

Hacker, B. R., Abers, G. A., & Peacock, S. M. (2003). Subduction factory 1. Theoretical mineralogy, densities, seismic wave speeds, and H_2O contents. *Journal of Geophysical Research*, *108*(B1), 2029. https://doi.org/10.1029/2001JB001127

Hardy, N. C. (1991). Tectonic evolution of the easternmost Panama Basin: Some new data and inferences. *Journal of South American Earth Sciences*, *4*(3), 261–269.

Hayes, G. P., Wald, D. J., & Johnson, R. L. (2012). Slab1.0: A three-dimensional model of global subduction zone geometries. *Journal of Geophysical Research*, *117*, B01302. https://doi.org/10.1029/2011JB008524

Heath, A. (2010). *SDX (Seismic Data eXplorer)*. Liverpool, UK: University of Liverpool. http://doree.esc.liv.ac.uk:8080/sdx

Herd, D. G., Youd, T. L., Meyer, H., Person, W. J., & Mendoza, C. (1981). The great Tumaco, Colombia earthquake of 12 December 1979. *Science*, *211*(4481), 441–445.

Hicks, S. P., Rietbrock, A., Ryder, I. M., Lee, C. S., & Miller, M. (2014). Anatomy of a megathrust: The 2010 M8. 8 Maule, Chile earthquake rupture zone imaged using seismic tomography. *Earth and Planetary Science Letters*, *405*, 142–155.

Hoskins, M. C., Meltzer, A., Font, Y., Agurto-Detzel, H., Vaca, S., Rolandone, F., et al. (2020). Triggered crustal earthquake swarm across subduction segment boundary after the 2016 Pedernales, Ecuador megathrust earthquake. *Earth and Planetary Science Letters*, *553*, 116620.

Husen, S., Kissling, E., & Flueh, E. R. (2000). Local earthquake tomography of shallow subduction in north Chile: A combined onshore and offshore study. *Journal of Geophysical Research*, *105*(B12), 28183–28198.

Hyndman, R. D. (1979). Poisson's ratio in the oceanic crust—A review. *Tectonophysics*, *59*(1–4), 321–333.

Institut De Physique Du Globe De Paris, & Ecole et Observatoire des Sciences de la Terre de Strasbourg. (1982). *GEOSCOPE, French Global Network of broad band seismic stations*. Institut de Physique du Globe de Paris (IPGP). Other/Seismic Network. http://doi.org/10.18715/GEOSCOPE.G

Jaillard, E., Hérail, G., Monfret, T., Díaz-Martínez, E., Baby, P., Lavenu, A., & Dumont, J. F. (2000). Tectonic evolution of the Andes of Ecuador, Peru, Bolivia and northernmost Chile. *Tectonic Evolution of South America*, *31*, 481–559.

Jaillard, E., Lapierre, H., Ordóñez, M., Toro, J., Amórtegui, A., & Vanmelle, J. (2009). Accreted oceanic terranes in Ecuador: Southern edge of the Caribbean Plate? *Geological Society, London, Special Publications*, *328*, 469–485.

Kanamori, H., & McNally, K. C. (1982). Variable rupture mode of the subduction zone along the Ecuador–Colombia coast. *Bulletin of the Seismological Society of America*, *72*(4), 1241–1253.

Kelleher, J. A. (1972). Rupture zones of large South American earthquakes and some predictions. *Journal of Geophysical Research*, *77*(11), 2087–2103.

Kendrick, E., Bevis, M., Smalley, R., Jr., Brooks, B., Vargas, R. B., Lauría, E., & Fortes, L. P. S. (2003). The Nazca–South America Euler vector and its rate of change. *Journal of South American Earth Sciences*, *16*(2), 125–131.

Koch, C. D., Lynner, C., Delph, J., Beck, S. L., Meltzer, A., Font, Y., et al. (2020). Structure of the Ecuadorian forearc from the joint inversion of receiver functions and ambient noise surface waves. *Geophysical Journal International*, *222*(3).1671–1685.

Kodaira, S., Iidaka, T., Kato, A., Park, J. O., Iwasaki, T., & Kaneda, Y. (2004). High pore fluid pressure may cause silent slip in the Nankai Trough. *Science*, *304*(5675), 1295–1298.

Kopp, H., Flueh, E. R., Papenberg, C., & Klaeschen, D. (2004). Seismic investigations of the O'Higgins Seamount Group and Juan Fernández Ridge: Aseismic ridge emplacement and lithosphere hydration. *Tectonics*, *23*, TC2009. https://doi.org/10.1029/2003TC001590

Lee, W. H. K., & Lahr, J. C. (1972). HYPO71: A computer program for determining hypocenter, magnitude, and first motion pattern of local earthquakes (No. 72-224). US Department of the Interior, Geological Survey, National Center for Earthquake Research.

León-Ríos, S., Agurto-Detzel, H., Rietbrock, A., Alvarado, A., Beck, S., Charvis, P., et al. (2019). 1D-velocity structure and seismotectonics of the Ecuadorian margin inferred from the 2016 Mw7. 8 Pedernales aftershock sequence. *Tectonophysics*, *767*, 228165.

Lonsdale, P. (1978). Ecuadorian subduction system. *AAPG Bulletin*, *62*(12), 2454–2477.

Lonsdale, P. (2005). Creation of the Cocos and Nazca plates by fission of the Farallon plate. *Tectonophysics*, *404*(3), 237–264.

Luzieux, L. D. A., Heller, F., Spikings, R., Vallejo, C. F., & Winkler, W. (2006). Origin and Cretaceous tectonic history of the coastal Ecuadorian forearc between 1 N and 3 S: Paleomagnetic, radiometric and fossil evidence. *Earth and Planetary Science Letters*, *249*(3–4), 400–414.

Lynner, C., Koch, C., Beck, S. L., Meltzer, A., Soto-Cordero, L., Hoskins, M. C., et al. (2020). Upper-plate structure in Ecuador coincident with the subduction of the Carnegie Ridge and the southern extent of large mega-thrust earthquakes. *Geophysical Journal International*, *220*(3), 1965–1977.

Marcaillou, B., Collot, J. Y., Ribodetti, A., d'Acremont, E., Mahamat, A. A., & Alvarado, A. (2016). Seamount subduction at the North-Ecuadorian convergent margin: Effects on structures, inter-seismic coupling and seismogenesis. *Earth and Planetary Science Letters*, *433*, 146–158.

Marcaillou, B., Spence, G., Wang, K., Collot, J. Y., & Ribodetti, A. (2008). Thermal segmentation along the N. Ecuador–S. Colombia margin (1–4 N): Prominent influence of sedimentation rate in the trench. *Earth and Planetary Science Letters*, *272*(1–2), 296–308.

Meissnar, R. O., Flueh, E. R., Stibane, F., & Berg, E. (1976). Dynamics of the active plate boundary in southwest Colombia according to recent geophysical measurements. *Tectonophysics*, *35*(1–3), 115–136.

Meltzer, A., Beck, S., Ruiz, M., Hoskins, M., Soto-Cordero, L., Stachnik, J. C., et al. (2019). The 2016 Mw 7.8 Pedernales, Ecuador, earthquake: RAPID response deployment. *Seismological Research Letters*, *90*(3), 1346–1354.

Meltzer, A., & Beck, S. L. (2016). *Pedernales earthquake aftershock deployment Ecuador*. International Federation of Digital Seismograph Networks. Dataset/Seismic Network. https://doi.org/10.7914/SN/8G_2016

Menant, A., Angiboust, S., Gerya, T., Lacassin, R., Simoes, M., & Grandin, R. (2020). Transient stripping of subducting slabs controls periodic forearc uplift. *Nature Communications*, *11*(1), 1–10. http://dx.doi.org/10.1038/s41467-020-15580-7

Mendoza, C., & Dewey, J. W. (1984). Seismicity associated with the great Colombia–Ecuador earthquakes of 1942, 1958, and 1979: Implications for barrier models of earthquake rupture. *Bulletin of the Seismological Society of America*, *74*(2), 577–593.

Michaud, F., Proust, J. N., Collot, J. Y., Lebrun, J. F., Witt, C., Ratzov, G., et al. (2015). Quaternary sedimentation and active faulting along the Ecuadorian shelf: Preliminary results of the ATACAMES Cruise (2012). *Marine Geophysical Research*, *36*(1), 81–98.

Michelini, A., & McEvilly, T. V. (1991). Seismological studies at Parkfield. I. Simultaneous inversion for velocity structure and hypocenters using cubic B-splines parameterization. *Bulletin of the Seismological Society of America*, *81*(2), 524–552.

Mothes, P. A., Nocquet, J. M., & Jarrín, P. (2013). Continuous GPS network operating throughout Ecuador. *Eos, Transactions American Geophysical Union*, *94*(26), 229–231.

Nakajima, J., Matsuzawa, T., Hasegawa, A., & Zhao, D. (2001). Three-dimensional structure of Vp, Vs, and Vp/Vs beneath northeastern Japan: Implications for arc magmatism and fluids. *Journal of Geophysical Research: Solid Earth*, *106*(B10), 21843–21857. http://dx.doi.org/10.1029/2000jb000008

Nocquet, J. M., Jarrin, P., Vallée, M., Mothes, P. A., Grandin, R., Rolandone, F., et al. (2017). Supercycle at the Ecuadorian subduction zone revealed after the 2016 Pedernales earthquake. *Nature Geoscience*, *10*(2), 145–149.

Nocquet, J. M., Mothes, P., & Alvarado, A. (2009). Geodesia, geodinámica y ciclo sísmico en Ecuador. In J. Y. Collot, et al. (Eds.), *Geologia y Geofisica Marina y Terrestre del Ecuador* (pp. 83–95).

Nocquet, J. M., Villegas-Lanza, J. C., Chlieh, M., Mothes, P. A., Rolandone, F., Jarrin, P., et al. (2014). Motion of continental slivers and creeping subduction in the northern Andes. *Nature Geoscience*, *7*(4), 287–291.

Ramírez, J. E. (1975). *Historia de los Terremotos en Colombia*. 2a edición, Bogotá, Colombia: Instituto Geográfico Agustín Codazzi.

Regnier, M., Font, Y., Charvis, P., Mercerat, D., Rietbrock, A., Ruiz, M., & Alvarado, A. (2016). *Pedernales*. International Federation of Digital Seismograph Networks. Dataset/Seismic Network. https://doi.org/10.7914/SN/XE_2016

Reyes, P., & Michaud, F. (2012). *Mapa Geológico de la Margen Costera Ecuatoriana (1:500000)*. Quito, Ecuador. EP, PetroEcuador & IRD.

Reynaud, C., Jaillard, É., Lapierre, H., Mamberti, M., & Mascle, G. H. (1999). Oceanic plateau and island arcs of southwestern Ecuador: their place in the geodynamic evolution of northwestern South America. *Tectonophysics*, *307*(3-4), 235–254.

Roecker, S. W., Iyer, H. M., & Hirahara, K. (1993). Tomography in zones of collision: Practical considerations and examples. *Seismic tomography: Theory and practice* (pp. 534–611). London, UK: Chapman & Hall.

Rolandone, F., Nocquet, J. M., Mothes, P. A., Jarrin, P., Vallée, M., Cubas, N., et al. (2018). Areas prone to slow slip events impede earthquake rupture propagation and promote afterslip. *Science Advances*, *4*(1), eaao6596.

Sallarès, V., Charvis, P., Flueh, E. R., & Bialas, J., & SALIERI Scientific Party. (2005). Seismic structure of the Carnegie ridge and the nature of the Galápagos hotspot. *Geophysical Journal International*, *161*(3), 763–788. http://dx.doi.org/10.1111/j.1365-246x.2005.02592.x

Sallarès, V., & Charvis, P. (2003). Crustal thickness constraints on the geodynamic evolution of the Galapagos Volcanic Province. *Earth and Planetary Science Letters*, *214*(3–4), 545–559.

Sallarès, V., & Ranero, C. R. (2005). Structure and tectonics of the erosional convergent margin off Antofagasta, north Chile (23°30′S). *Journal of Geophysical Research*, *110*, B06101. https://doi.org/10.1029/2004JB003418

Segovia, M. (2001). *Título de Ingeniera Geología (tesis): El sismo de Bahía del 4 de agosto de 1998: Caracterización del mecanismo de ruptura y análisis de la sismicidad en la zona costera*. Quito, Ecuador: Escuela Politécnica Nacional.

Segovia, M., Alvarado, A., Collot, J. Y., Sallares, V., & Pazmiño, N. (2009). Breve análisis de la sismicidad y del campo de esfuerzos en el Ecuador. In *Geología y Geofisica Marina y Terrestre del Ecuador: Desde la costa continental hasta las Islas Galápagos* (pp. 131–149).

Segovia, M., Font, Y., Régnier, M., Charvis, P., Galve, A., Nocquet, J. M., et al. (2018). Seismicity distribution near a subducting seamount in the central Ecuadorian subduction zone, space–time relation to a slow-slip event. *Tectonics*, *37*, 2106–2123. https://doi.org/10.1029/2017TC004771

Sennson, J. L., & Beck, S. L. (1996). Historical 1942 Ecuador and 1942 Peru subduction earthquakes and earthquake cycles along Colombia–Ecuador and Peru subduction segments. *Pure and Applied Geophysics*, *146*(1), 67–101.

Soto-Cordero, L., Meltzer, A., Bergman, E., Hoskins, M., Stachnik, J. C., Agurto-Detzel, H., et al. (2020). Structural control on megathrust rupture and slip behavior: Insights from the 2016 Mw 7.8 Pedernales Ecuador earthquake. *Journal of Geophysical Research: Solid Earth*, *125*, e2019JB018001. https://doi.org/10.1029/2019JB018001

Spakman, W., & Nolet, G. (1988). Imaging algorithms, accuracy and resolution in delay time tomography. In *Mathematical geophysics* (pp. 155–187). Dordrecht: Springer.

Storchak, D. A., Di Giacomo, D., Bondár, I., Engdahl, E. R., Harris, J., Lee, W. H., et al. (2013). Public release of the ISC–GEM global instrumental earthquake catalogue (1900–2009). *Seismological Research Letters*, *84*(5), 810–815.

Thurber, C. H. (1983). Earthquake locations and three-dimensional crustal structure in the Coyote Lake area, central California. *Journal of Geophysical Research*, *88*(B10), 8226–8236.

Thurber, C. H. (1993). Local earthquake tomography: Velocities and Vp/Vs-theory. In H. M. Iyer & K. Hirahara (Eds.), *Seismic tomography: Theory and practice* (pp. 563–583). London: Chapman and Hall.

Thurber, C. H., Atre, S. R., & Eberhart-Phillips, D. (1995). Three-dimensional Vp and Vp/Vs structure at Loma Prieta, California, from local earthquake tomography. *Geophysical Research Letters*, *22*(22), 3079–3082.

Toomey, D. R., & Foulger, G. R. (1989). Tomographic inversion of local earthquake data from the Hengill-Grensdalur Central Volcano Complex, Iceland. *Journal of Geophysical Research: Solid Earth*, *94*(B12), 17497–17510. http://dx.doi.org/10.1029/jb094ib12p17497

Trenkamp, R., Kellogg, J. N., Freymueller, J. T., & Mora, H. P. (2002). Wide plate margin deformation, southern Central America and northwestern South America, CASA GPS observations. *Journal of South American Earth Sciences*, *15*(2), 157–171.

Vaca, S., Régnier, M., Bethoux, N., Alvarez, V., & Pontoise, B. (2009). Sismicidad de la región de Manta: Enjambre sísmico de Manta-2005. In *Geologia y Geofisica Marina y Terrestre del Ecuador Desde la Costa Continental Hasta las Islas Galapagos* (pp. 151–166).

Vaca, S., Vallée, M., Nocquet, J. M., Battaglia, J., & Régnier, M. (2018). Recurrent slow slip events as a barrier to the northward rupture propagation of the 2016 Pedernales earthquake (Central Ecuador). *Tectonophysics*, *724*, 80–92.

Vallée, M., Nocquet, J. M., Battaglia, J., Font, Y., Segovia, M., Regnier, M., et al. (2013). Intense interface seismicity triggered by a shallow slow slip event in the Central Ecuador subduction zone. *Journal of Geophysical Research: Solid Earth*, *118*, 2965–2981. https://doi.org/10.1002/jgrb.50216

von Huene, R., & Culotta, R. (1989). Tectonic erosion at the front of the Japan Trench convergent margin. *Tectonophysics*, *160*(1–4), 75–90.

von Huene, R., Ranero, C. R., & Vannucchi, P. (2004a). Generic model of subduction erosion. *Geology*, *32*(10), 913–916.

von Huene, R., Ranero, C. R., & Watts, P. (2004b). Tsunamigenic slope failure along the Middle America Trench in two tectonic settings. *Marine Geology*, *203*(3–4), 303–317.

von Huene, R., Ranero, C. R., Weinrebe, W., & Hinz, K. (2000). Quaternary convergent margin tectonics of Costa Rica, segmentation of the Cocos Plate, and Central American volcanism. *Tectonics*, *19*(2), 314–334.

Wang, K., & Bilek, S. L. (2011). Do subducting seamounts generate or stop large earthquakes? *Geology*, *39*(9), 819–822.

Watts, A. B., Koppers, A. A., & Robinson, D. P. (2010). Seamount subduction and earthquakes. *Oceanography*, *23*(1), 166–173.

White, R. S., McKenzie, D., & O'Nions, R. K. (1992). Oceanic crustal thickness from seismic measurements and rare earth element inversions. *Journal of Geophysical Research*, *97*(B13), 19683–19715.